Systematic study of azimuthal anisotropy in Cu+Au collisions at $\sqrt{s_{\mathrm{NN}}} = 200$ GeV

Takafumi Niida[*]and Sergei A. Voloshin[†]

Wayne State University

April 16, 2018

Abstract

This note presents the analysis detail of the directed flow as well as the elliptic flow and higher-order flow up to 4th-order in Cu+Au collisions. For comparison, the odd and even components of the directed flow in Au+Au collisions were also studied. Results are compared with the viscous hydrodynamic model and a multi-phase transport model.

Contents

---

[*]niida@bnl.gov

[†]voloshin@wayne.edu

1

1   Introduction

In this note, we present the systematic study of anistropic flow in Cu+Au collisions. The Cu+Au collisions provide the intrinsic asymmetric desnsity distribution in the transverse plane of the overlap region across the colliding nuclei as well as asymmetric spectator distribution. Our previous study presented charge-dependent directed flow to see the effect of the initial electric field created by the difference in the number of spectator protons in two nuclei. In this study, we focus on charge-independent anistropic flow from 1st-order upto 4th-order, using charged particles and identified charged pions, kaons, and protons. Results are compared with results from Au+Au collisions and Pb+Pb collisions (only for v_1) and are also comapred with the viscous hydrodymamic model and a Multi-Phase Transport model.

2   Analysis

2.1   Event and track selection

Data from run12 Cu+Au collisions at $\sqrt{s_{NN}} = 200$ GeV was used for this analysis. Bad run rejection, event selection, and track selection are same as the analysis on charge-dependent directed flow. The detailed can be found in the analysis note [1]. All basic cuts are summarized here:

Run and Event selection for run12 Cu+Au

- cuAu_production_2012, P15ie
- Trigger ID used: 410008 and 410005
- removed bad runs: 13139063, 13139064, 13139065, 13139066, 13139067, 13139072, 13139073, 13139074, 13139080, 13143037, 13145005, 13147030
- $|v_z| < 30$ cm
- $|v_r| < 2$ cm from the center (vertex position in transverse plane)
- $|v_z - v_z^{vpd}| < 3$ cm
- Cut based on the correlation between RefMult and TofMult

Run and Event selection for run10 Au+Au

- AuAu200_production, P10ik
- Trigger ID used: 260001, 260011, 260021, and 260031
- removed bad runs: see Ref. [1]
- $|v_z| < 30$ cm
- $|v_r| < 2$ cm from the center (vertex position in transverse plane)

- $|v_z - v_z^{vpd}| < 3$ cm
- Cut based on the correlation between RefMult and TofMult

Track selection

- $0.15 < p_T < 5$ GeV/c
- $|\eta| < 1$
- nHitsFit>=15
- nHistFit/nHitsPoss>=0.52
- gDCA<3 cm

In the reconstruction of the event plane, the p_T range is limited to $0.15 < p_T < 2$ GeV/c.

2.2   Centrality definition

Centrality definition used for Cu+Au collisions is same as the previous study [1]. Please see the analysis note for the detail. Centrality for run10 Au+Au collisions was determined based on RefMultCorr class.

2.3   Event plane reconstruction

For flow measurements, event planes were reconstructed by ZDC-SMD, BBC, TPC, and EEMC using the following formula:

$$\Psi_n = \frac{1}{n} \tan^{-1}(\frac{Q_{n,y}}{Q_{n,x}}) \tag{1}$$

$$Q_{n,x} = \sum w_i \cos(n\phi_i)/\sqrt{\sum w_i} \tag{2}$$

$$Q_{n,y} = \sum w_i \sin(n\phi_i)/\sqrt{\sum w_i} \tag{3}$$

where w_i is a weight of a particle i for TPC and a segment or tower i for ZDC, BBC, and EEMC. In case using TPC, p_T of tracks ($0.15< p_T <2$ GeV/c) was used as the weight. The adc or energy ($E_T < 2$ GeV/c) were used for BBC and EEMC. The details of event plane calibration and its QA are described in [1]. The ϕ in Eq. 2 and Eq. 3 is azimuthal angle of particles and n denotes the order of harmonics.

Event plane resolution was estimated via three sub event method [8, 9]:

$$\text{Res}\{\Psi_n^A\} = \sqrt{\frac{\langle \cos n(\Psi_n^A - \Psi_n^B)\rangle \langle \cos n(\Psi_n^A - \Psi_n^C)\rangle}{\langle \cos n(\Psi_n^B - \Psi_n^C)\rangle}} \tag{4}$$

where A, B, and C denote different subevents in East (Au-going) or West (Cu-going) sides. The resolution of 1$^{\text{st}}$-order event plane is same as the charge-dependent v_1

analysis [1]. For higher-orders, we used TPC subevents from the following η regions; $-1 < \eta < -0.4$, $|\eta| < 0.2$, and $0.4 < \eta < 1$. At least the η-gap more than 0.2 was taken among subevents. When using the EEMC ($1 < \eta < 2$), the TPC subevent of $0.4 < \eta < 1$ was replaced with the EEMC subevent. Figure 1 shows event plane resolutions of Ψ_2, Ψ_3, and Ψ_4 for TPC and EEMC subevents and resolutions of the first-order event plane for ZDCSMD east or west sides. Res$\{\Psi_2\}$ is ~ 0.4, Res$\{\Psi_3\}$ is ~ 0.25, and Res$\{\Psi_4\}$ is ~ 0.1 at maximum. The first-order event plane is clearly larger for Au-going direction (east side) but the similar trend can be seen for higher-orders.
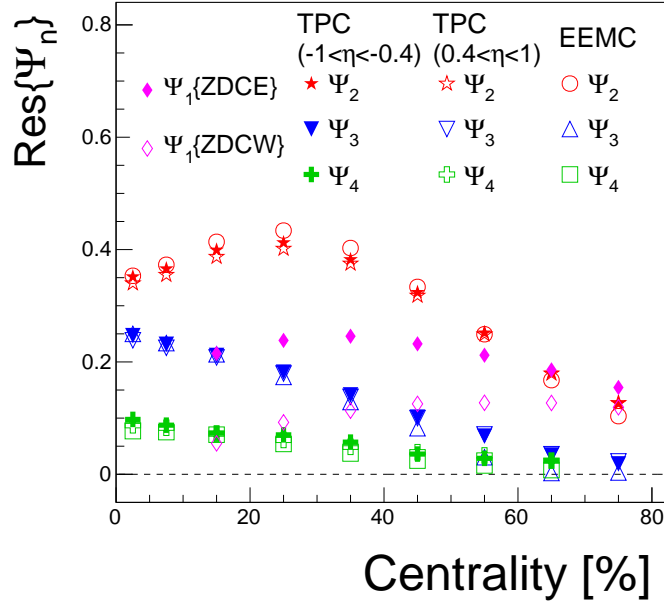

Fig. 1: Resolution of event planes for ZDCSMD, TPC subevents and EEMC

2.4   Particle Identification

Particle identification of charged particles was performed by using the information of an ionization energy loss in TPC (dE/dx) combining with the time-of-flight (TOF) detector. Figure 2 shows the mass square (m^2) from TOF vs $n\sigma_\pi$ from TPC. Three peaks of pions, kaons, and protons are clearly seen. Since the separation of those particles are clearer in m^2, the particle selection was basically done based on m^2 when the TOF information is available but the $n\sigma$ from TPC was also used for an additional constraint. When the TOF information is not available, only the TPC information was used. The cuts for particle selection used in this analysis are summarized below:

If the TOF information is available:

- π: $m_\pi^2 \pm 2\sigma_{m_\pi^2}$, veto on $m_{K(p)}^2 \pm 2\sigma_{m_{K(p)}^2}$, and $|n\sigma_\pi| < 3$ for $0.2 < p < 3.4$ GeV/c

- K: $m_K^2 \pm 2\sigma_{m_K^2}$, veto on $m_\pi^2 \pm 2.5\sigma_{m_\pi^2}$ and $m_p^2 \pm 2\sigma_{m_p^2}$, and $|n\sigma_K| < 3$ for $0.2 < p < 2.6$ GeV/c

- p: $m_p^2 \pm 2\sigma_{m_p^2}$, veto on $m_{\pi(K)}^2 \pm 2\sigma_{m_{\pi(K)}^2}$, and $|n\sigma_p| < 3$ for $0.4 < p < 3.4$ GeV/c

and if the TOF information is not available:

- π: $|n\sigma_\pi^\pi| < 2$ for $0.2 < p \leq 0.6$ GeV/c
  $|n\sigma_\pi^\pi| < 2$ and $|n\sigma_\pi^K| > 2$ for $0.6 < p < 0.7$ GeV/c

- K: $|n\sigma_K^K| < 2$ for $0.2 < p \leq 0.5$ GeV/c
  $|n\sigma_K^K| < 2$ and $|n\sigma_K^\pi| > 3$ for $0.5 < p < 0.7$ GeV/c

- p: $|n\sigma_p^p| < 2$ for $0.4 < p \leq 0.9$ GeV/c
  $|n\sigma_p^p| < 2$ and $|n\sigma_p^\pi| > 3$ for $0.9 < p < 1.2$ GeV/c

where $n\sigma_a^b$ denotes the normalized standard deviation of particle b in the $n\sigma$ distribution of particle a. Figure 3 shows the mass square versus momentum multiplied by the sign of electric charge of particles, where the dashed lines show ideal mass squares for π, K, and p. The Gaussian fit was applied each momentum bin and the fitting results, i.e. mean and sigma, are shown in Fig. 4. The lines with the data points show the polynomial fitting functions. In Fig 3, 2σ lines from each particle mass peaks are plotted.

The upper limits of the momentum ranges shown above are determined based on purities of each particle. Figure 5 shows m^2 distribution with Gaussian fitting functions in $0.5 < p < 0.6$ GeV/c and $2.5 < p < 2.6$ GeV/c. The shaded area in the right plot shows kaon samples selected by the requirements of $(m^2 - m_K^2) < 2\sigma$ and $(m^2 - m_\pi^2) > 2.5\sigma$. The purity was estimated assuming each peaks follow Gaussian distribution as shown in Fig. 6. The true distributions may not be Gaussian distribution and/or there would be some fraction of the background which presumably comes from mis-reconstruction of tracks. Further studies can be found in the appendix. Based on this assumption, the purity drops down to ∼97% and in the estimate of the worst case it

could be ~90% (see appendix) at higher p_T. Figure 7 shows $n\sigma$ distributions for π, K, and p. Similarly the shaded areas show selected particles following the selection criteria shown above, where the purities are kept to be >99% for pions, >98% for kaons and protons.
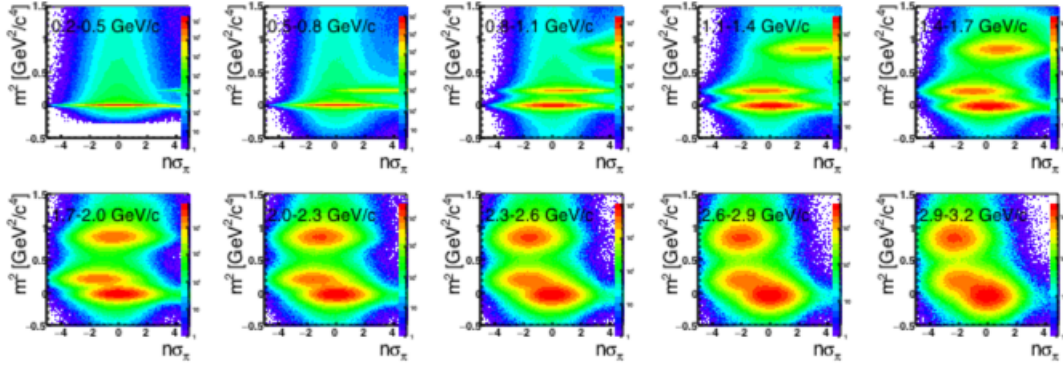

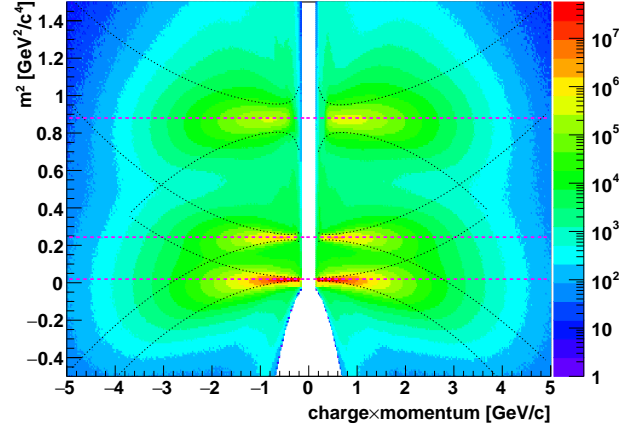Fig. 2: Mass square vs $n\sigma_\pi$ for different momentum bins

Fig. 3: Mass square vs momentum multiplied by the sign of electric charge of particles. Dashed lines show an ideal mass square of π, K, and p and dotted curves show 2σ lines from the peak of each particle.
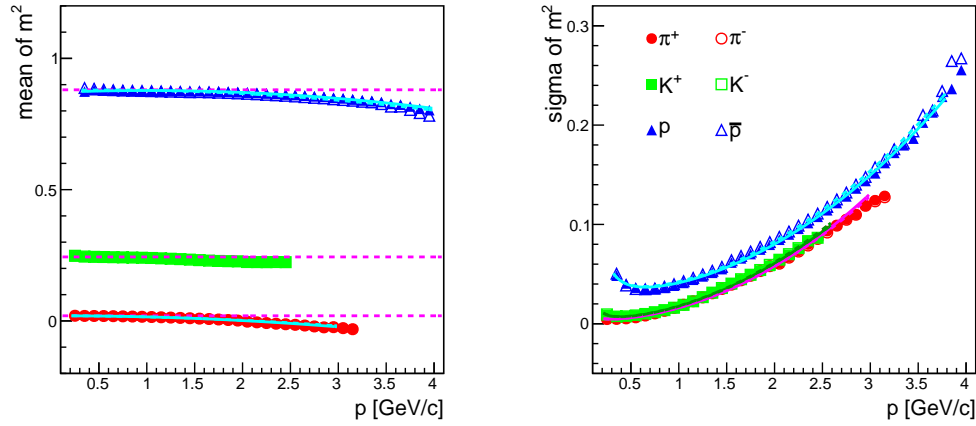

Fig. 4: (Left)Mean of mass square distribution for each particle as a function of momentum. (Right)Gaussian width of mass square distribution for each particle. Filled (open) symbols show positively (negatively) charged particles.
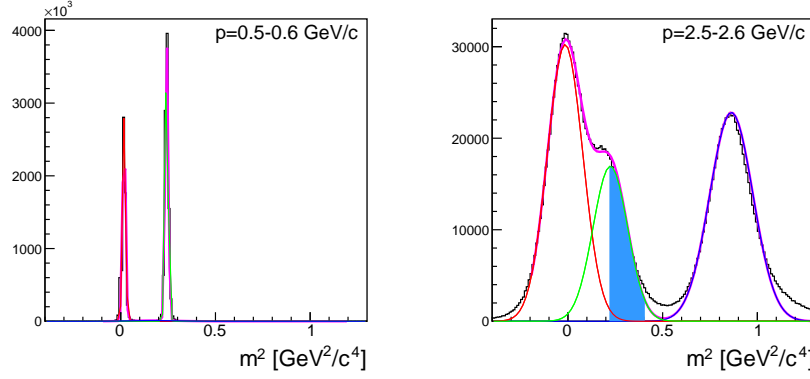
Fig. 5: m^2 distribution in $0.5< p <0.6$ GeV/c and $2.5< p <2.6$ GeV/c after applying $|n\sigma_K| < 3$, where each Gaussian components obtained by the fit are shown. Shaded area shows kaon samples selected by $(m^2 - m_K^2) < 2\sigma$ and $(m^2 - m_\pi^2) > 2.5\sigma$.
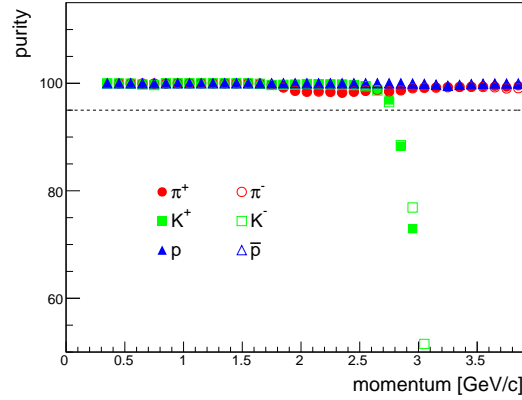

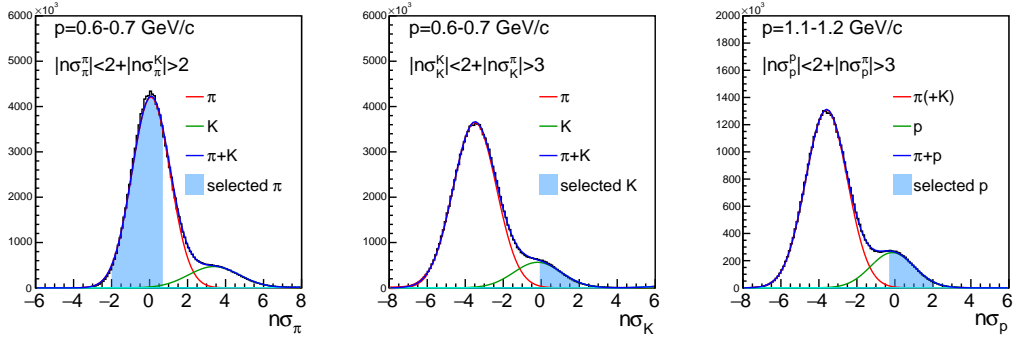Fig. 6: TOF-PID Purity as a function of momentum, where the dashed line shows 95%.

Fig. 7: $n\sigma$ distributions of π, K, and p for specific momentum ranges shown in the figures. Solid lines show Gaussian components of each particles obtained from the fit. Shaded areas show particles selected by requiring a veto cut from the neighboring particle. When selecting pions (kaons or protons), kaon (pion) veto cut was applied.

2.5   Flow measurements

2.5.1   Event plane method

Azimuthal anisotropic flow v_n was measured with the event plane method:

$$v_n = \frac{\langle \cos n(\phi - \Psi_n) \rangle}{\text{Res}(\Psi_n)} \tag{5}$$

where ϕ denotes azimuthal angle of particles and $\langle \, \rangle$ means an average over all particles in all events. As described in the previous section, the event planes of TPC subevents were reconstructed in $-1 < \eta < -0.4$ and $0.4 < \eta < 1$. To avoid auto-correlation and reduce the non-flow effects like back-to-back jet, v_n was measured taking the η gap more than 0.4 between the event plane and particles of interest. Since v_n measured with respect to backward and forward event planes are consistent with each other, the average of both results was used as final results.

2.5.2   Scalar product method

The scalar product method was also checked in this analysis.

$$v_n = \frac{\langle \boldsymbol{u} \cdot \boldsymbol{Q}_n^A / N^A \rangle}{\sqrt{\dfrac{\langle \boldsymbol{Q}_n^B / N^B \cdot \boldsymbol{Q}_n^C / N^C \rangle}{\langle \boldsymbol{Q}_n^A / N^A \cdot \boldsymbol{Q}_n^B / N^B \rangle \langle \boldsymbol{Q}_n^C / N^C \cdot \boldsymbol{Q}_n^A / N^A \rangle}}} \tag{6}$$

where $\boldsymbol{Q}_n$ is a flow vector defined in Eq. (2) and Eq. (3) and $\boldsymbol{u}$ is a unit vector of a particle of interest. The index A, B, and C denote subevents from different η region and N is $N = \sum_i w_i$

2.5.3   Three-point correlator for directed flow

Also, for the directed flow, three-point correlator [10] was tested for cross check:

$$v_1 = \frac{\langle \cos(\phi + \Psi_1^A - 2\Psi_2^B) \rangle}{\text{Res}(\Psi_1^A) \times \text{Res}(\Psi_2^B)} \tag{7}$$

where A and B denote different subevents with different η coverages. The $\text{Res}(\Psi_1^A)$ was estimated by using a double harmonic correlation between Ψ_1 and the reaction plane Ψ_{RP} based on the following equation:

$$\langle \cos(2(\Psi_1 - \Psi_{RP})) \rangle = \frac{\langle \cos(2(\Psi_1 - \Psi_2)) \rangle}{\text{Res}(\Psi_2)}. \tag{8}$$

The resolution function for certain harmonics can be expressed analytically [9], therefore one can calculate the $\langle \cos(\Psi_1 - \Psi_{RP}) \rangle = \text{Res}(\Psi_1)$ using Eq. 8. Figure 8 shows raw correlation between Ψ_1^A and Ψ_2^B, $\text{Res}(\Psi_2^B)$ obtained by three subevent method, the
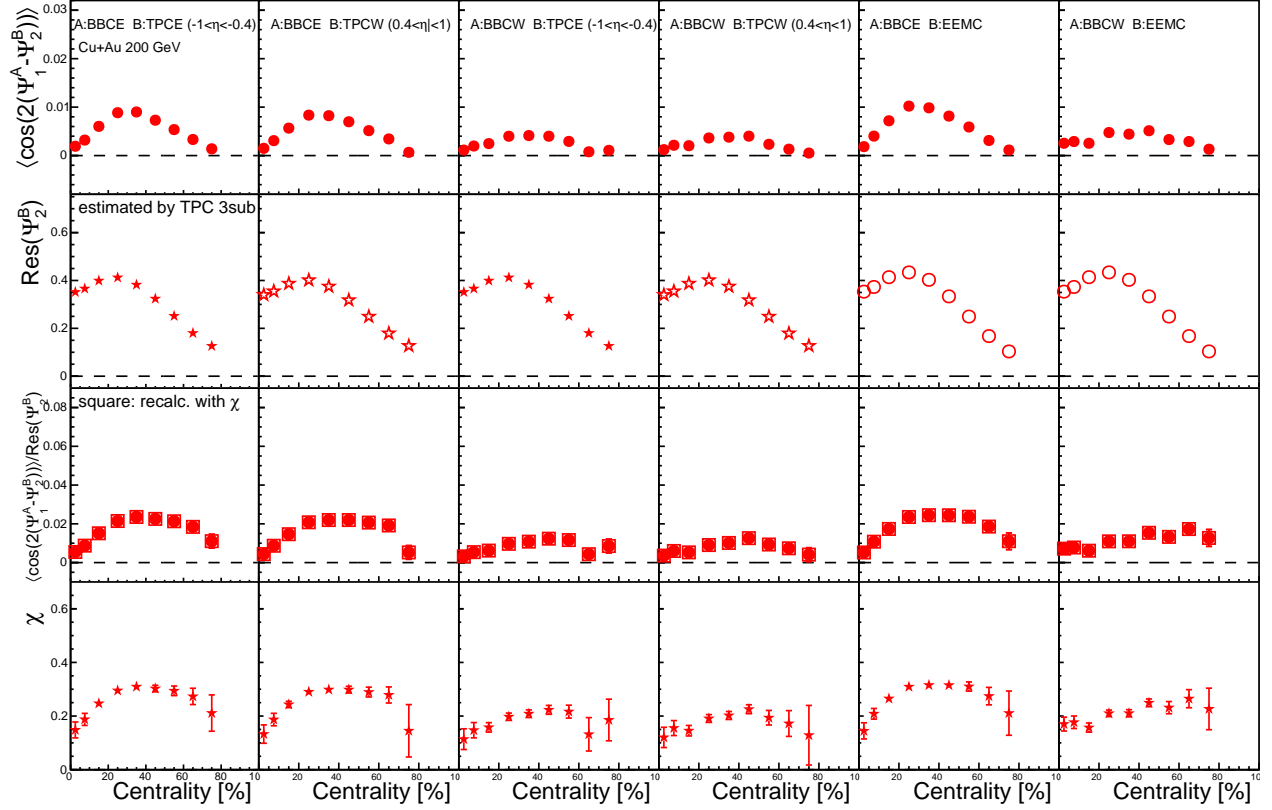
Fig. 8: Correlation between Ψ_1^A and Ψ_2^B, $\mathrm{Res}(\Psi_2^B)$, their ratio, and the parameter χ in the analytical formula of Ref. [9], as a function of centrality, for different subevent combinations.

ratio of Eq. 8, and the parameter χ in the analytical formula of Ref. [9], for different subevent combinations of A and B. In this analysis, the three largest correlation of $\Psi_1^A - \Psi_2^B$ were used, which are BBCE-TPCE($-1 < \eta < -0.4$), BBCE-TPCW($0.4 < \eta < 1$), and BBCE-EEMC. When using TPC subevent, particles of interest were taken from different rapidity from that subevent. To make a fair comparison with the event plane method where the particles of interest are taken from $-1 < \eta < 1$, average of $v_1\{3\}$ with BBCE-TPCE and BBCE-TPCW were used as a final result. Difference from $v_1\{3\}$ with BBCE-EEMC was included in the systematic uncertainty. Figure 9 shows the resolution of Ψ_1 obtained by Eq. 8. The $\mathrm{Res}(\Psi_1)$ estimated from the three-subevent method using the spectator planes are also shown together for comparison and systematically smaller values.
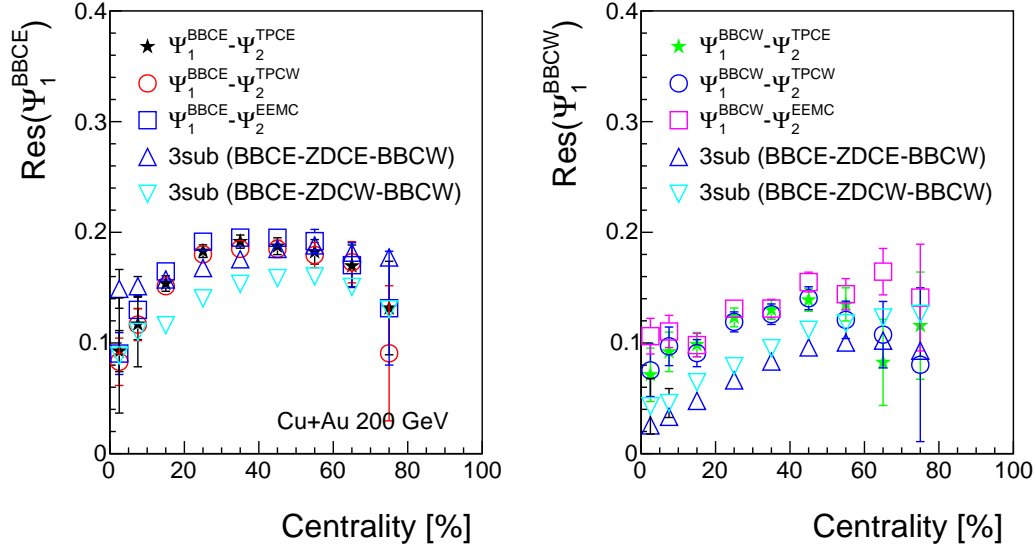
Fig. 9: Res(Ψ_1) obtained from Ψ_1-Ψ_2 correlation based on Eq. 8 as a function of centrality.

2.6   Systematic uncertainties

Systematic uncertainties were estimated by the variations of track quality cut and z-vertex cut. Also, the difference of v_n between TPC subevents and EEMC event planes was taken into account. The sources of the systematic uncertainties are listed below:

- dca<3 cm or dca<2 cm
- nHitsFit>15 or nHitsFit>20
- $|v_z|$ <30 cm or $|v_z|$ <20 cm
- different event plane: TPC sub-events or EEMC for v_n (n≥2)

For v_1 measurements with the event plane method, the variation of the event plane resolutions from different three subevent combinations were taken into account as explained in the previous study [1]. For v_1 with the three-point correlator, the effect of different event plane combinations were taken into account in the systematic uncertainty. As described in [1], trigger efficiency correction was applied.

2.6.1   Unidentified charged particles

Figure 10 shows v_2 as a function of p_T with 10% step centrality (5% step in most central events), where one of sources of the systematic uncertainties is varied. Top and middle panels show positive and negative charged particles, and bottom panels show

the average of both charges. Since there is no significant difference between positive
and negative charges, charged combined results were used as final results. Figure 11
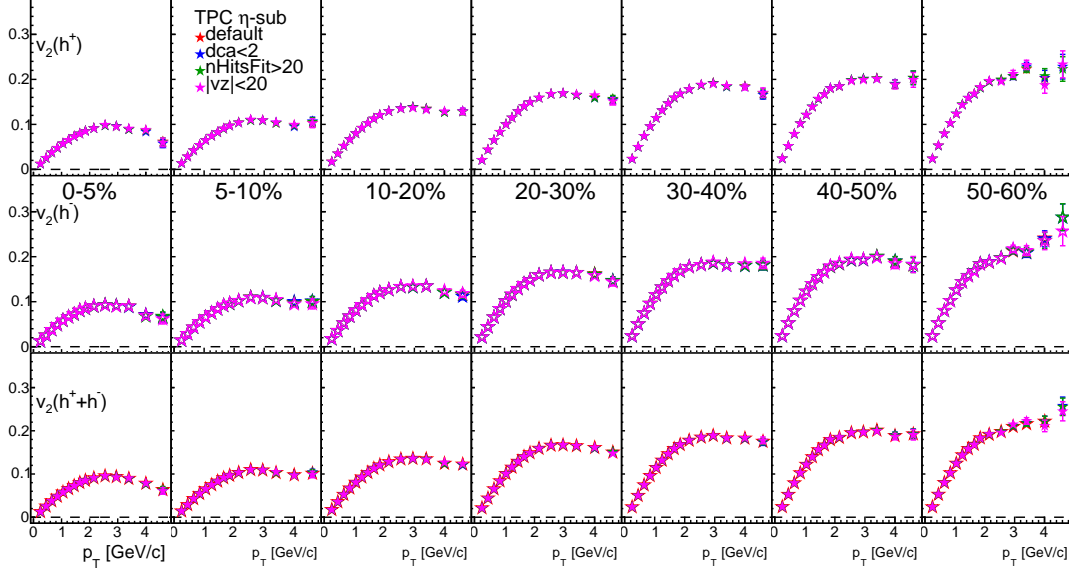and Figure 12 are the same plots for v_3 and v_4.

Fig. 10: v_2 as a function of p_T in 0-5%, 5-10%, and 10% step centrality when varying the
systematic source. Top, middle, and bottom panels show positive charged particles, negative
charged particles, and charge combined results.

Figure 13 shows $v_2(p_T)$ in different centrality bins measured with TPC η and
EEMC. Lower panels show a difference between both results in percentile. To esti-
mate the systematic uncertainty from the event plane determination, the v_2 difference
was fitted with a constant function. Fitting results were assigned to the systematic
uncertainty. Figure 14 and Figure 15 show the same plots for v_3 and v_4.

Figure 16 shows $v_1\{3\}(p_T)$ for different conditions of track and event cuts. Figure 17
shows $v_1\{3\}(p_T)$ for different event plane combinations, where one of BBCs for Ψ_1 and
one of TPC subevents for Ψ_2 are used. Final systematic uncertainties are defined as a
quadratic sum of the difference from the default cut condition. But for the uncertainty
from the event plane the corrected v_n moves to the same direction as shown in Fig. 13,
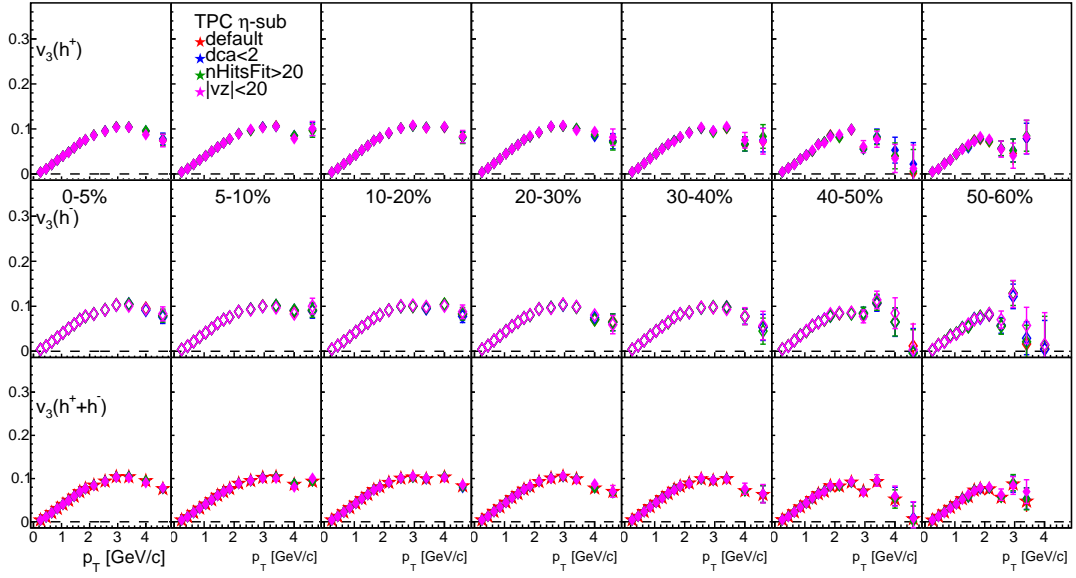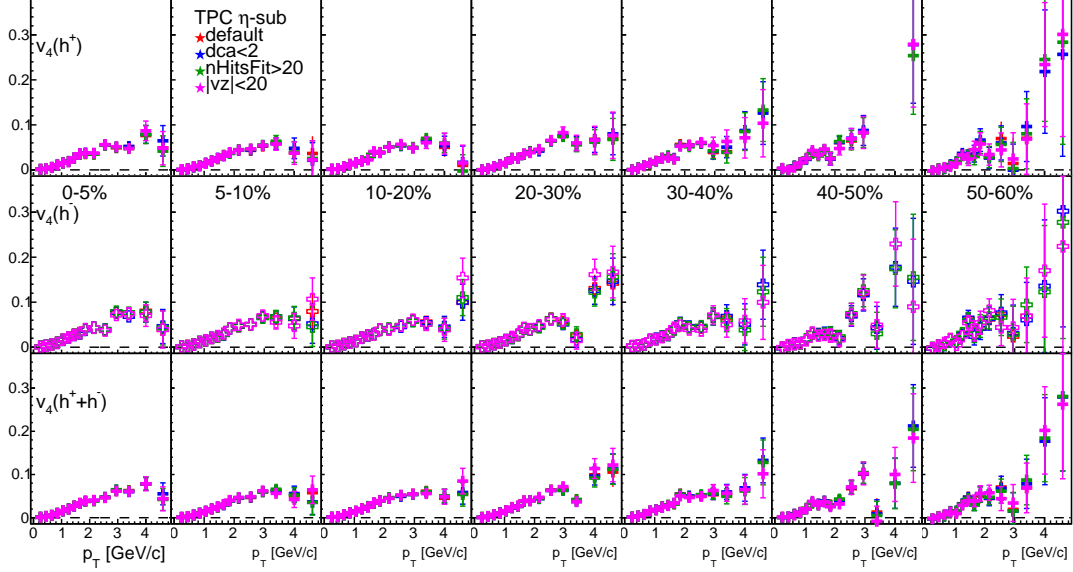14, 15. Therefore it will be plotted separately in final figures.

Fig. 11: v_3 as a function of p_T in 0-5%, 5-10%, and 10% step centrality when varying the systematic source. Top, middle, and bottom panels show positive charged particles, negative charged particles, and charge combined results.
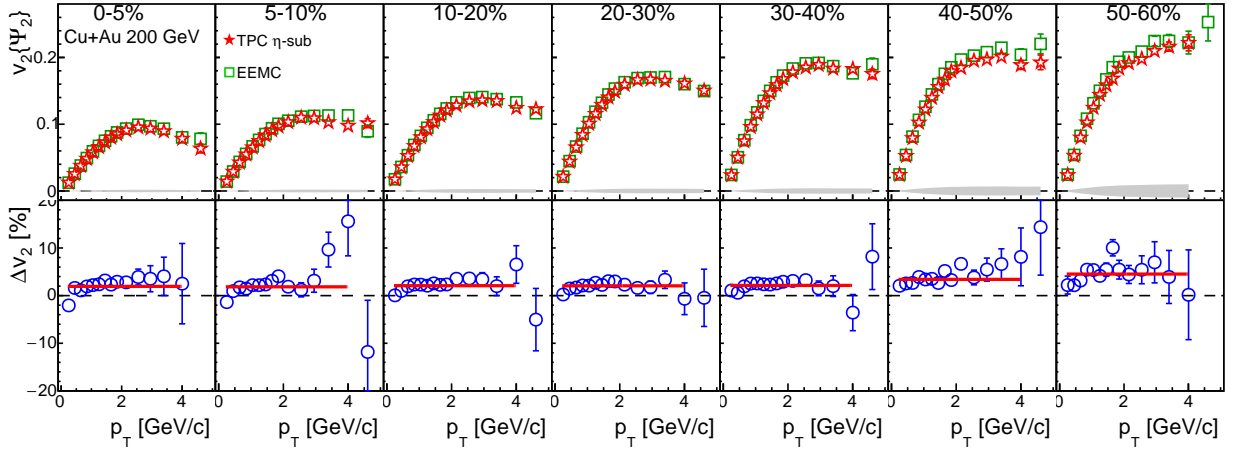
Fig. 12: v_4 as a function of p_T in 0-5%, 5-10%, and 10% step centrality when varying the systematic source. Top, middle, and bottom panels show positive charged particles, negative charged particles, and charge combined results.
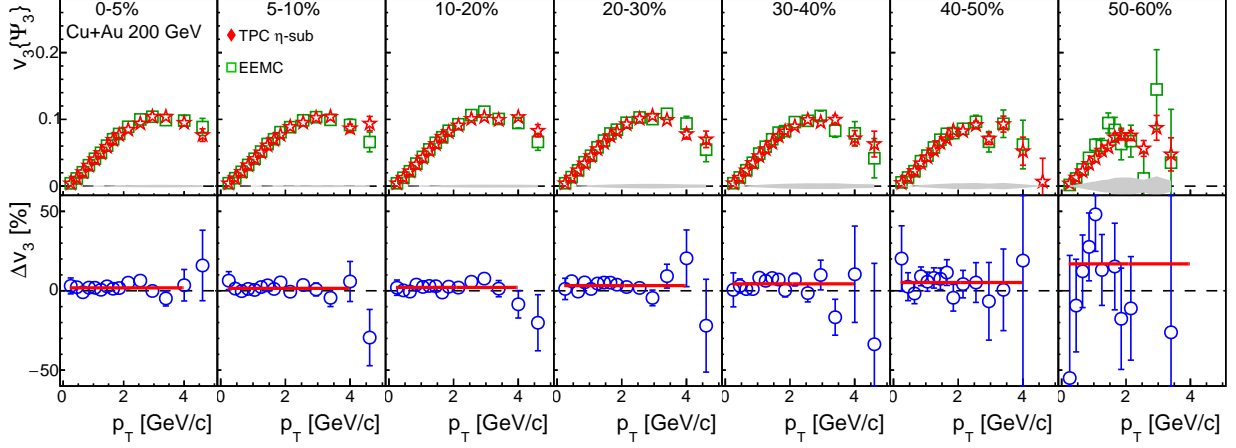

Fig. 13: Upper panels show v_2 as a function of p_T in 0-5%, 5-10%, and 10% step centrality measured with TPC η-sub and EEMC. Gray shaded bands around $v_2 = 0$ denote systematic uncertanties from the event plane determination. Lower panels show the difference between both results in percentile.
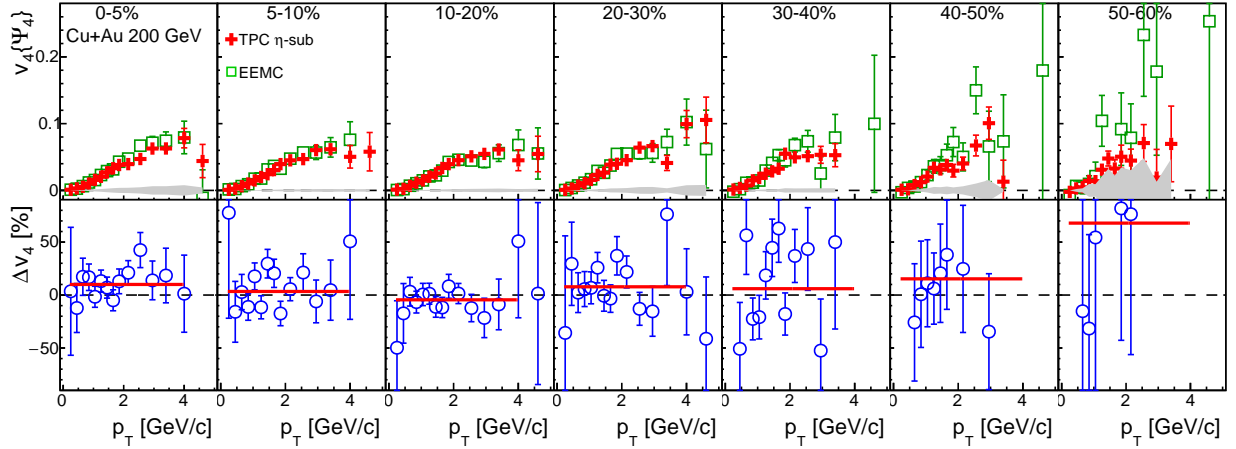
Fig. 14: v_3 as a function of p_T in 0-5%, 5-10%, and 10% step centrality measured with TPC η-sub and EEMC. Gray shaded bands around $v_3 = 0$ denote systematic uncertanties from the event plane determination. Lower panels show the difference between both results in percentile.
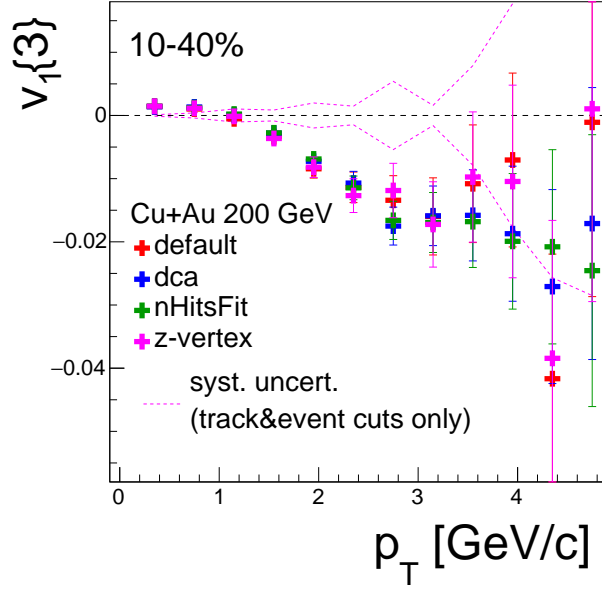

Fig. 15: v_4 as a function of p_T in 0-5%, 5-10%, and 10% step centrality measured with TPC η-sub and EEMC. Gray shaded bands around $v_4 = 0$ denote systematic uncertanties from the event plane determination. Lower panels show the difference between both results in percentile.

Fig. 16: $v_1\{3\}$ as a function of p_T in 10-40% centrality bin for different track and event cuts in Cu+Au collisions.
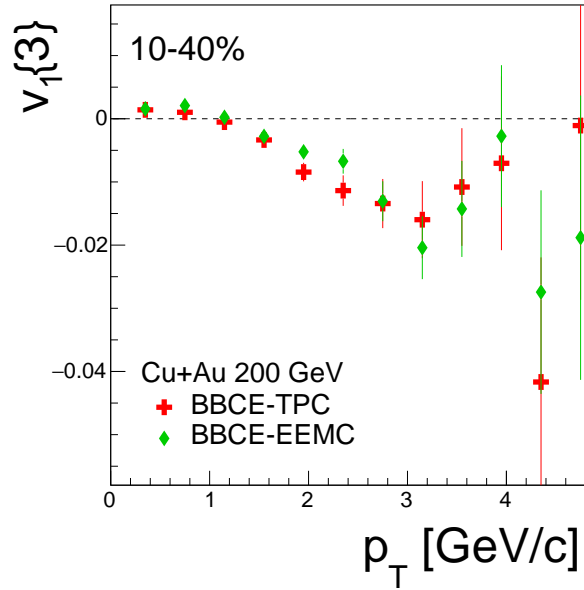

Fig. 17: $v_1\{3\}$ as a function of p_T in 10-40% centrality bin for two different event plane combinations in Cu+Au collisions.

2.6.2   Identified charged particles

In the same way as v_n of charged particles, the systematic uncertainties were estimated for identified particles, $\pi^+ + \pi^-$, $K^+ + K^-$, and $p + \bar{p}$. In addition to that, a variation of PID cut was also considered in the systematic uncertainty to include the effect of purity. Figure 18 shows v_1 of charge combined pions, kaons, and protons as a function of p_T for variations of track quality cuts, PID selection, and zvertex cut. Figure 19 shows differences of v_1 for charge pions, kaons, and protons from the results with default cut when the event plane resolution was estimated by using different combination of three subevents. The difference reachs about 15%-20% and this is the largest systematic uncertainty for v_1. Figure 20 shows differences in v_2, v_3, and v_4 from the results with default cut for variations of track quality cuts, PID selection, and zvertex cut. These effects are below 5% for v_2 and v_3 but become larger for v_4 although the statistical fluctuations also become larger. Figure 21 shows v_2, v_3, and v_4 of charged pions, kaons, and protons measured using TPC η subevent or EEMC subevent as the event plane.
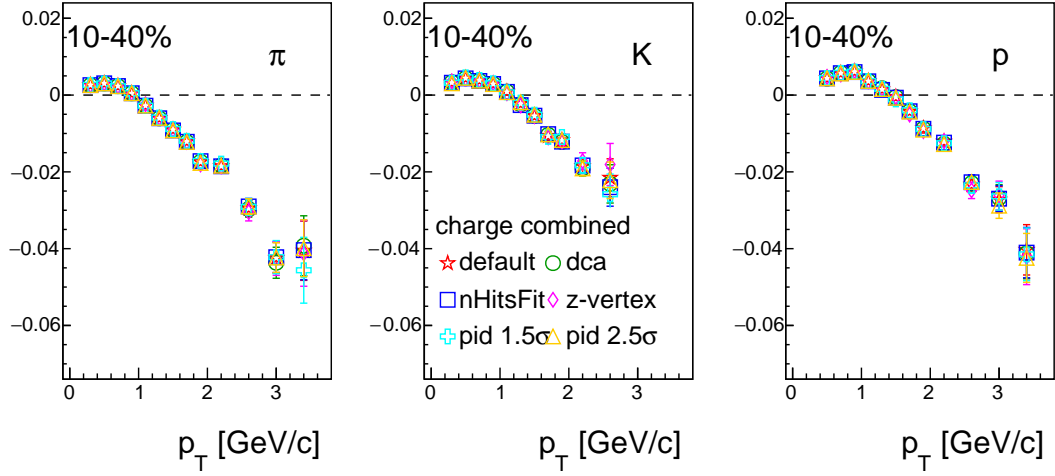

Fig. 18: v_1 of $\pi^+ + \pi^-$, $K^+ + K^-$, and $p + \bar{p}$ as a function of p_T in 10-40% centrality bin for different track and event cuts.
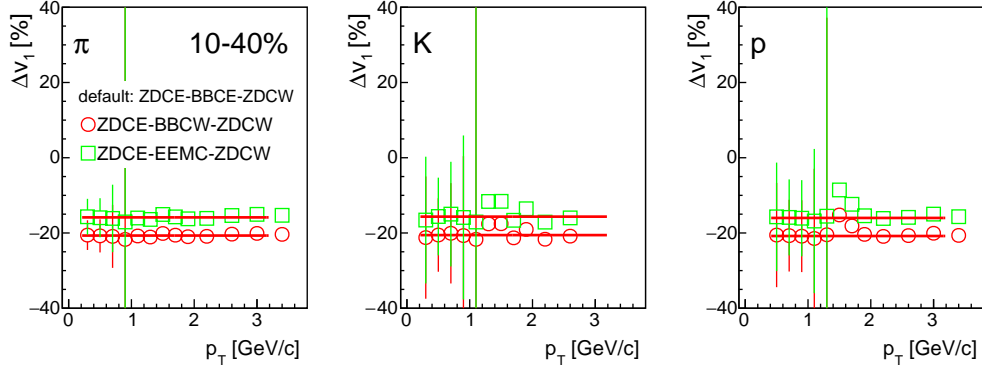
Fig. 19: Difference of $v_1(p_T)$ of $\pi^+ + \pi^-$, $K^+ + K^-$, and $p + \bar{p}$ measured with TPC η-sub and EEMC subevents in 10-40% centrality bin.
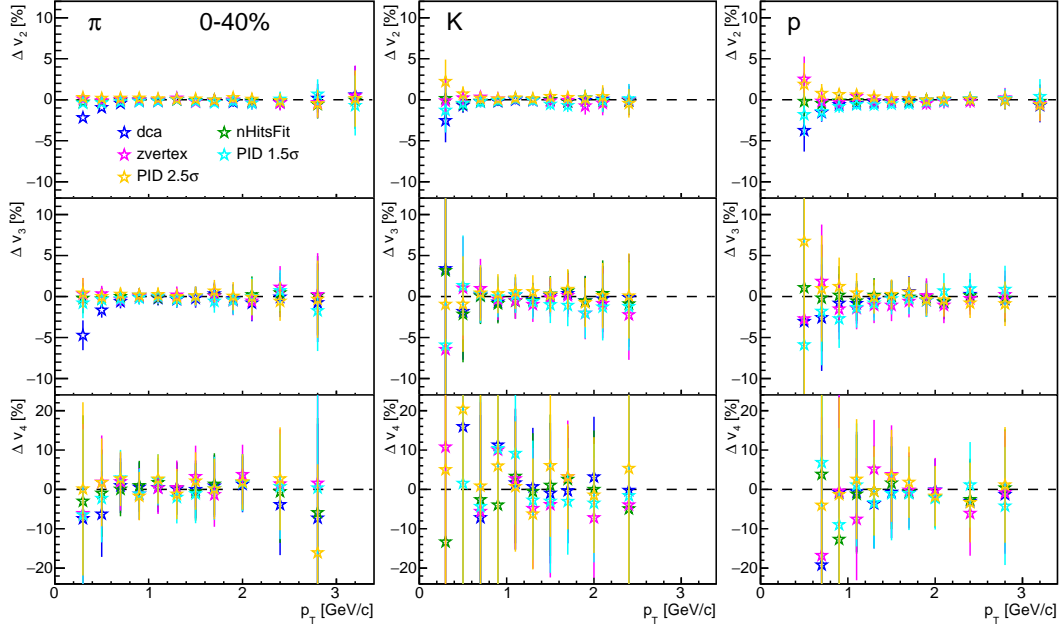

Fig. 20: Difference of $v_n(p_T)$ of $\pi^+ + \pi^-$, $K^+ + K^-$, and $p + \bar{p}$ between different track and event cuts in 10-40% centrality bin.
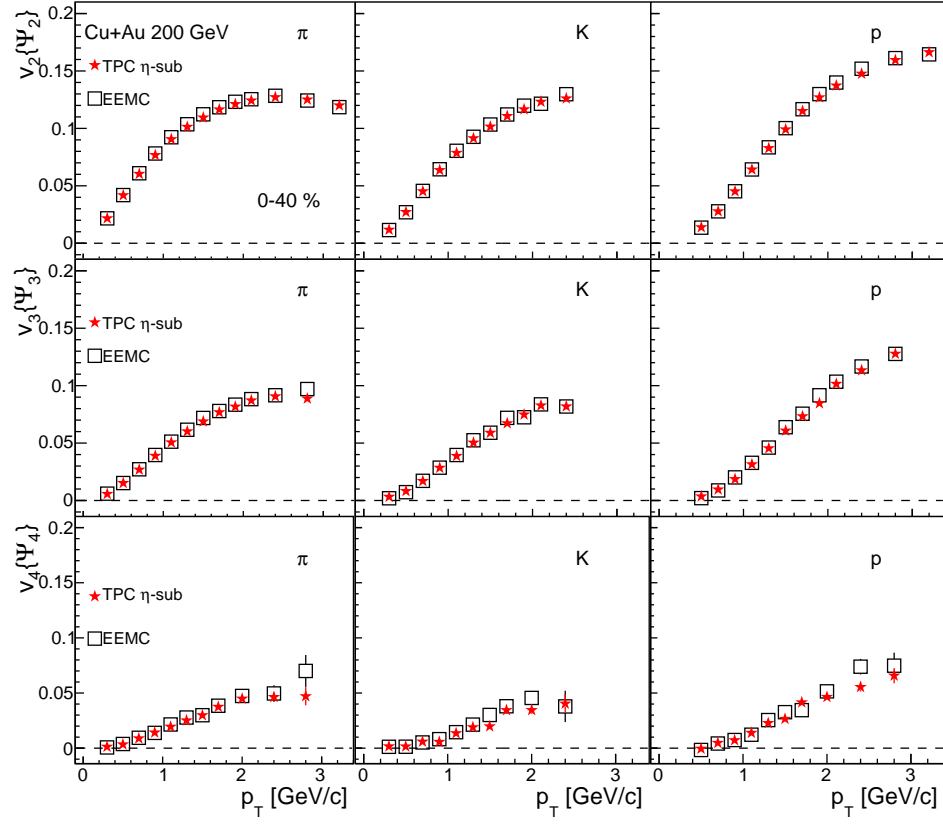
Fig. 21: v_n of $\pi^+ + \pi^-$, $K^+ + K^-$, and $p + \bar{p}$ measured with TPC η-sub and EEMC subevents as a function of p_T in 10-40% centrality bin.

3   Results

3.1   Unidentified charged particles

3.1.1   Directed flow

Directed flow was measured with respect to the spectator planes determined by ZD-CSMD in east and west sides. Figure 22 shows v_1 as a function of pseudorapidity for 10%-40% centrality bin in Cu+Au and Au+Au collisions. Here Ψ_{SP} for projectile (forward rapidity, Cu-going direction) is defined to be positive to follow the convention of the past v_1 analyses. Because of a negative correlation of $\langle\cos(\Psi_{\mathrm{SP}}^p - \Psi_{\mathrm{SP}}^t)\rangle$, the sign of v_1 measured with Ψ_{SP}^t is flipped. In both systems, there is a finite difference between $v_1\{\Psi_{\mathrm{SP}}^p\}$ and $v_1\{\Psi_{\mathrm{SP}}^p\}$. This suggests that there is a component of v_1 derived from the fluctuations (rapidity even component in symmetric collisions) in addition to the conventional v_1 (rapidity odd component in symmetric collisions).
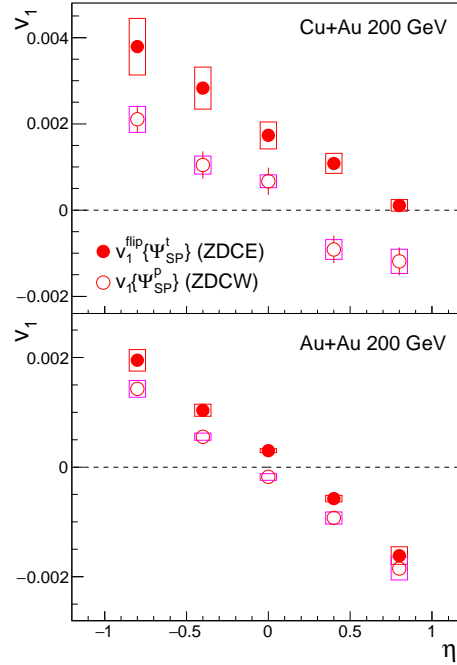

Fig. 22: $v_1(\eta)$ of charged particles with respect to the spectator planes from ZDCSMD East and ZDCSMD West for 10%-40% centrality in Cu+Au and Au+Au collisions.

The odd and even component of v_1 can be defined as [3]:

$$v_1^{\text{odd(conv)}} = (v_1\{\Psi_{\text{SP}}^p\} - v_1\{\Psi_{\text{SP}}^t\})/2 \tag{9}$$

$$v_1^{\text{even(fluc)}} = (v_1\{\Psi_{\text{SP}}^p\} + v_1\{\Psi_{\text{SP}}^t\})/2 \tag{10}$$

where $\Psi_{\text{SP}}^p(t)$ is an azimuthal angle of projectile (target) spectator plane. Note that the "projectile" spectator goes to forward direction (Cu-going direction in Cu+Au collisions). The notation of "odd" and "even" for v_1 components can be used only for symmetric collisions, therefore the words of "conv" (conventional) and "fluc" (fluctuation) are used for Cu+Au collisions.

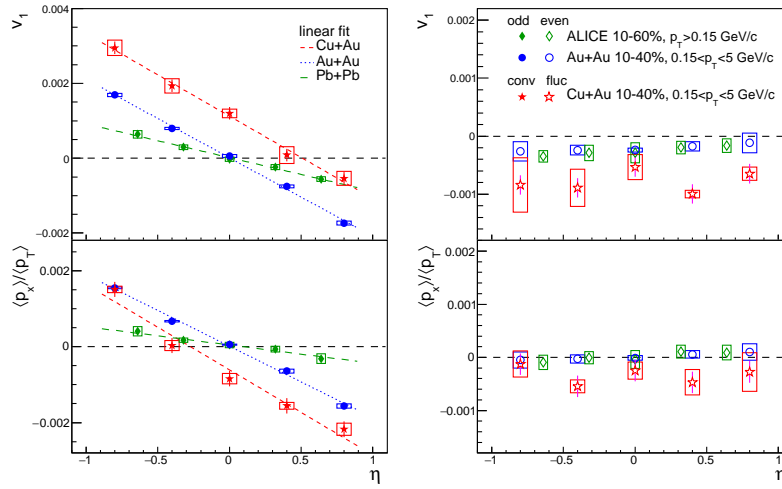
Fig. 23: Rapidity-odd (conventinal) and rapidity-even (fluctuation) component of $v_1(\eta)$ and $p_x(\eta)$ of charged particles for 10%-40% centrality in Au+Au, Cu+Au and Pb+Pb collisions.

Figure 23 shows $v_1^{\text{odd(conv)}}$ and $v_1^{\text{even(fluc)}}$ for 10%-40% centrality bin in Cu+Au, Au+Au, and Pb+Pb collisions from the ALICE experiment [3]. The mean transverse momentum projected to the spectator plane ($\langle p_x \rangle = \langle p_T \cos(\phi - \Psi_{\text{SP}}) \rangle$) was aslo measured in the same way as v_1. The v_1^{oddconv} was fitted with a linear function to guide the eye. The slope of $v_1^{\text{odd(conv)}}$ in Cu+Au is similar to that in Au+Au but is shifted to the forward direction. The slopes in Cu+Au and Au+Au are steeper than that in Pb+Pb, which is a similar energy dependnece as observed in RHIC BES data [4]. On the other hand, $\langle p_x \rangle$ in Cu+Au has a steeper slope than that in Au+Au and its magnitude becomes larger in Cu-going direction. This could be understood by the momentum balance to compensate fewer particles in Cu-going direction than in Au-going direction. The magnitude of v_1^{even} in Au+Au is similar to that in Pb+Pb, suggesting a similar magnitude of the initial dipole-like density fluctuations. The $\langle p_x \rangle$ in Au+Au

and Pb+Pb is consistent with zero as expected from a characteristic feature of the dipole flow. The magnitude of v_1^{even} in Cu+Au is larger than those in Au+Au and Pb+Pb. It may indicate a larger
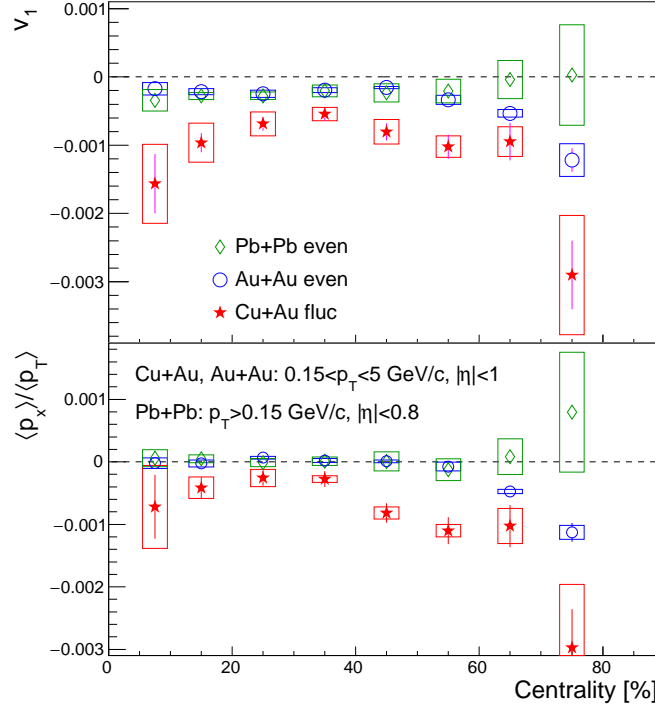

Fig. 24: Centrality dependence of rapidity-odd (conventional) and rapidity-even (fluctuation) component of $v_1(\eta)$ and $p_x(\eta)$ in 10%-40% centrality in Au+Au, Cu+Au and Pb+Pb collisions.

Figure 24 shows the even (fluctuation) component of v_1 and p_x as a function of centrality in Au+Au, Cu+Au, and Pb+Pb [3] collisions. The v_1^{even} shows a weak centalty dependence and good agreement between Au+Au and Pb+Pb collisions except peripheral events. The p_x^{even} is consistent with zero as expected from the nature of the dipole flow. The v_1^{fluc} and p_x^{fluc} in Cu+Au collisions show a similar centality dependnece and are larger than Au+Au collisions in magnitude.

Figure 25 shows the charge-dependent transverse momentum projected to the spectator plane, p_x, and the difference betweenn positively and negatively charged particles, as a function of centrality in Au+Au and Cu+Au collisions. Both results were integrated over the pseudorapidity range from -1 to 1. Non-zero values of Δp_x are observed in Au+Au collisions when using one of spectator planes and their signs are opposite. As reported in the STAR previous paper [4], the odd component of v_1 is different especially between proton and anti-proton even in Au+Au collisison at $\sqrt{s_{NN}} = 200$ GeV.
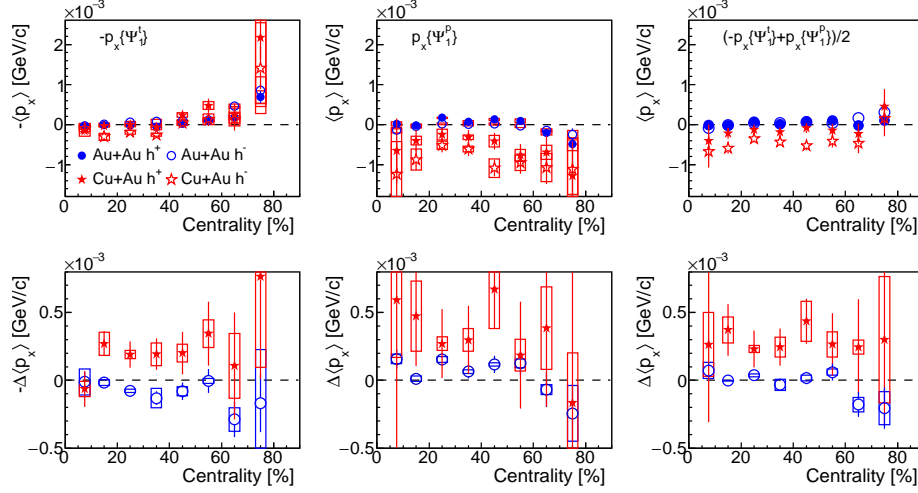
Fig. 25: p_x and Δp_x as a function of centrality in Au+Au and Cu+Au collisions, measured with respect to target (left) and projectile (middle) spectator planes. Right panels show the average of results from target and projectile spectator planes considering the sign of two spectator planes.

In the symmetric collisions, the rapidity-odd component of $p_x(v_1)$ should be cancelled out by integrating over $-1 < \eta < 1$ unless there is non-uniform detector efficinecy along psuedorapidity which may also depend on charge of particles. Note that the tracking efficiency depending on p_T and η was taken account into. Therefore, the observed difference might be due to the residiual odd component. Note that there is no charge dependence in the even component of v_1 [2]. By taking average of the results from two spectator planes as shown in right panels, such a residual odd-component should be cancelled out but the charge difference should remain if it exists. No significant difference was observed between both signs in this case. In Cu+Au case, the conventinal component of p_x (also v_1) is asymmetric over rapidity in magnitude, both conventional and fluctuation components of p_x would be included in the left two panels. When taking the average as shown in the right panels, the conventional components would be cancelled out as mentioned above, but the charge dependence should remain if it exists. A finite difference is observed in the region of 10%-60% centrality. The effect is consistent with the expectation from the initial electric field and charge-dependent v_1 in our previous study [2]. Figure 26 is a final plot for our proposed paper which is the same as the right panels in Fig. 25.

Figure 27 shows p_T dependence of $v_1^{\text{odd(conv)}}$ and $v_1^{\text{even(fluc)}}$ of charged particles for five centrality bins, which were measured based on the Eq. 5. To obtain v_1^{odd} in Au+Au collisions, the sign of v_1 was flipped when $\eta < 0$. In both $v_1^{\text{odd(conv)}}$ and $v_1^{\text{even(fluc)}}$, there is a sign change around $p_T = 1\text{-}1.5$ GeV/c and the magnitude of v_1 becomes smaller
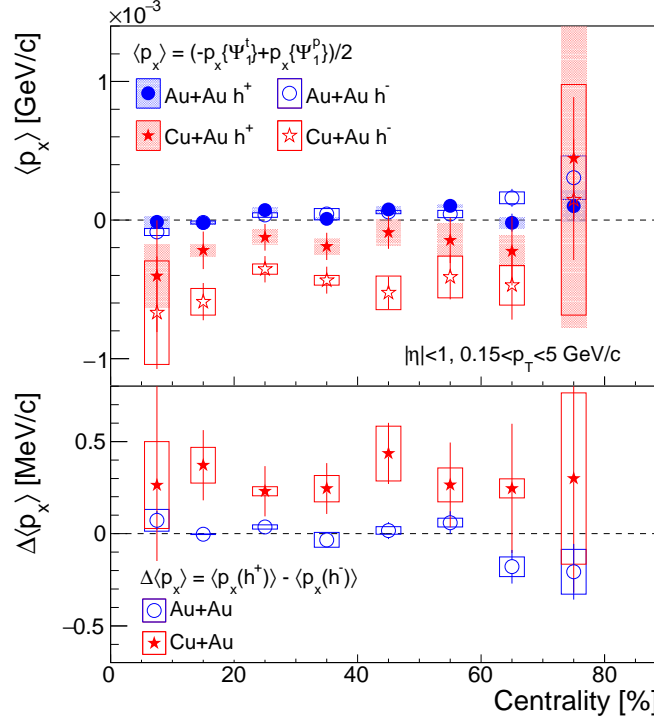
Fig. 26: Centrality dependence of rapidity-odd (conventional) and rapidity-even (fluctuation) component of $v_1(\eta)$ and $p_x(\eta)$ in 10%-40% centrality in Au+Au, Cu+Au and Pb+Pb collisions.

in more peripheral collisions. The Cu+Au v_1^{conv} has the opposite sign to the Au+Au v_1^{odd} with the currrent definition and way of the v_1 measurements, as seen in Fig. 23.

Figure 28 shows $v_1\{3\}$ measured with three-point correlator compared to v_1^{covn} and v_1^{fluc} with the event plane method using the spectator planes for 10-40% centrality bin in Cu+Au collisions. The $v_1\{3\}$ is consistent with the v_1^{conv} at $p_T < 2$ GeV/c and there is a finite differen at higher p_T, although the uncertainties are large. The large systematic uncertainty in the $v_1\{3\}$ comes from the combination of the event planes.

3.1.2   Higher-order flow

Figure 29 shows p_T dependence of higher-order flow v_n for seven centrality bins. v_2 shows a strong centrality dependence and becomes largest around 40-60% centrality. v_3 and v_4 show a weaker centrality dependence compared to v_2. These trends are similar to what has been observed in Au+Au collisions at $\sqrt{s_{NN}} = 200$ GeV. In Fig. 30, the v_n for two selected p_T bins ($\langle p_T \rangle = 1.2$ GeV/c and $\langle p_T \rangle = 1.2$ GeV/c) are plotted as function of the collision centrality and the number of participants from the Glauber
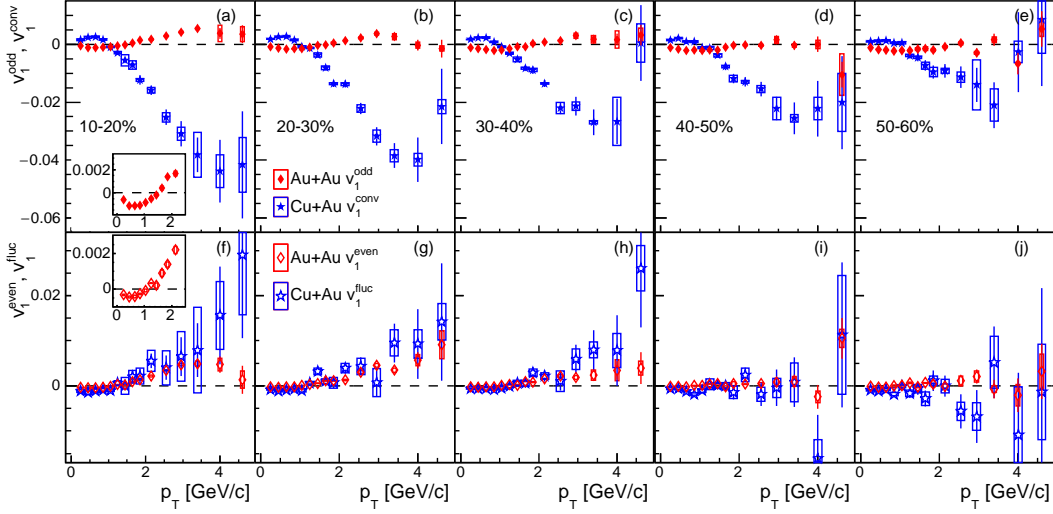
Fig. 27: $v_1^{\mathrm{odd(conv)}}$ and $v_1^{\mathrm{even(fluc)}}$ as a function of p_T for different centrality bins in Au+Au and Cu+Au collisions.

simulation. Results in Au+Au collisions from the STAR and PHENIX experiments are compared [13, 14, 15]. All v_n show a rough agreement between two different systems in the same centrality because v_2 is proportial to the initial eccentricity ε_2 (the centrality roughly corresponds to ε_2). and the v_3 and v_4 have less centrality dependence. When comapring the data in the same N_{part} window, the v_3 seems to be more consistent between two systems. It may be natural if v_3 predominantly originates from the initial density fluctuations which should be correlated to N_{part}. The Cu+Au v_4 is slightly lower than the Au+Au v_4. Figure 31 shows the same plots as bottom one in Fig. 30 with the systematic uncertainties.

3.1.3   Comparison with PHENIX

PHENIX have recently submitted a paper on Cu+Au flow [11]. Our results are compared to the PHENIX results, v_2 in Figure 32 and v_3 in Figure 33. For v_2, both results are consistent with each other in $p_T < 2$ GeV/c within their systematic uncertainties. There is systematically a difference above $p_T = 2$ GeV/c, which is probably due to different non-flow contribution to v_2. Our $v_2\{\mathrm{TPC}\}$ has η-gap of 0.4 while the PHENIX v_2 has η-gap of 2.65 (Central arm: $|\eta| < 0.35$, BBC: $3< |\eta| <3.9$) and therefore the PHENIX results would have less non-flow effect. In Fig. 34, our $v_2\{\mathrm{BBC}\}$ (STAR BBC: $3.3< |\eta| <5$) is compared and consistent with the PHENIX even in $p_T > 2$ GeV/c. The v_3 are consistent between both experiments within the systematic uncertainties.
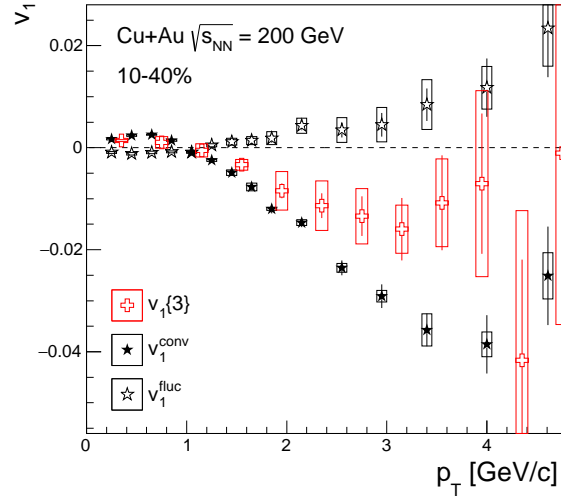
Fig. 28: Charge-combined $v_1(p_T)$ measured with the three-point correlator and the event plane method for 10-40% centrality in Cu+Au collisions.

3.1.4   Comparison with a hydrodynamic model

Figure 35 shows v_2 and v_3 compared with the calculations by event-by-event viscous hydrodynamical model [12] in 0-5% and 20-30% centrality bins. The model calculates v_n with two different η/s (0.08 and 0.16). The model qualitatively reproduces the data. In 0-5%, the data slightly favors the case with $\eta/s = 0.08$, but in 20-30% the data are almost between two calculations.

3.1.5   Comparison with AMPT model

A Multi-Phase Transport (AMPT) model was also compared with our results. We used AMPT models of v1.26t5 for default version and v2.26t5 for string meting version. To be consistent with the experimental analysis, the event plane reconstruction and flow measurements were performed in the same way. Figure 36 shows comparisons of v_2, v_3, and v_4 with AMPT calculations for the default version and string melting version with the parton cross section $\sigma_{pp} = 1.5$ mb and $\sigma_{pp} = 3$ mb. The AMPT model qualitatively describes all v_n results at p_T below 3 GeV/c for different centraliti bins and the data seems to be between the results of the default version and $\sigma_{pp} = 1.5$ mb.
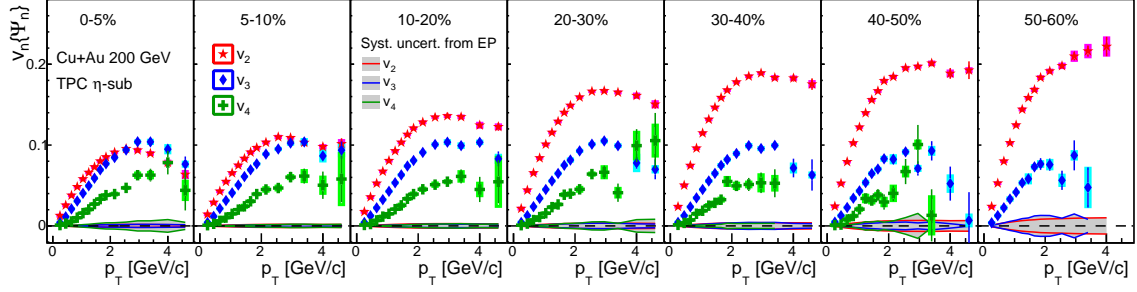
Fig. 29: Higher-order azimuthal anisotropies v_n as a function of p_T for different centrality bins.
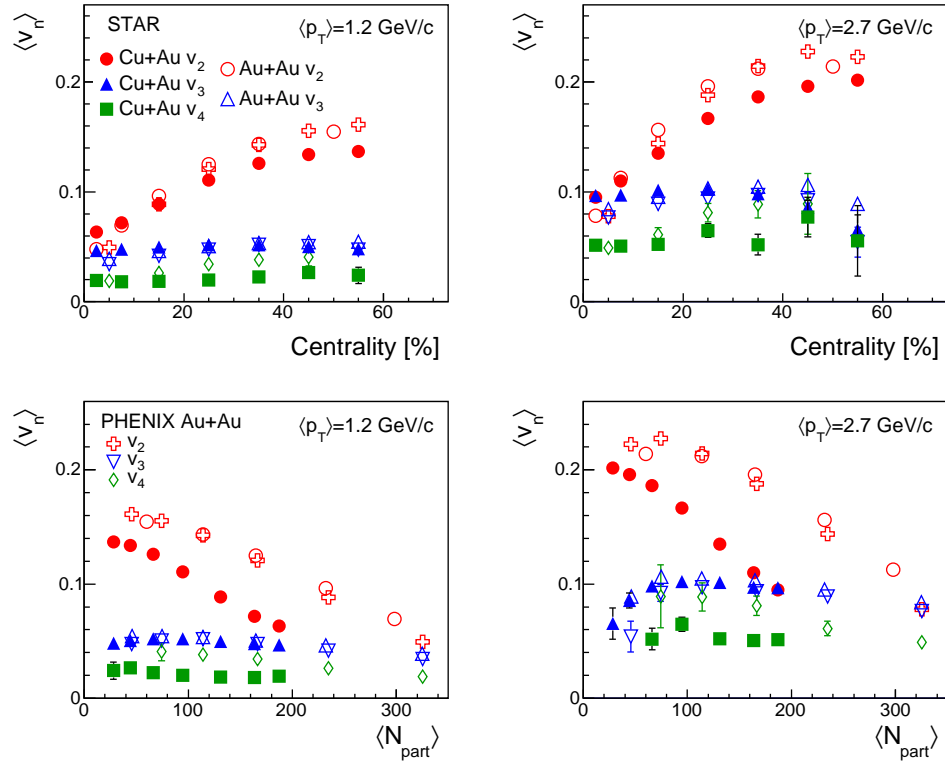

Fig. 30: v_n as a function of the collision centrality (top) and the number of participants N_{part} (bottom) for two selected p_T bins. Results for Au+Au collisions from the STAR [13, 14] and PHENIX [15] are compared.
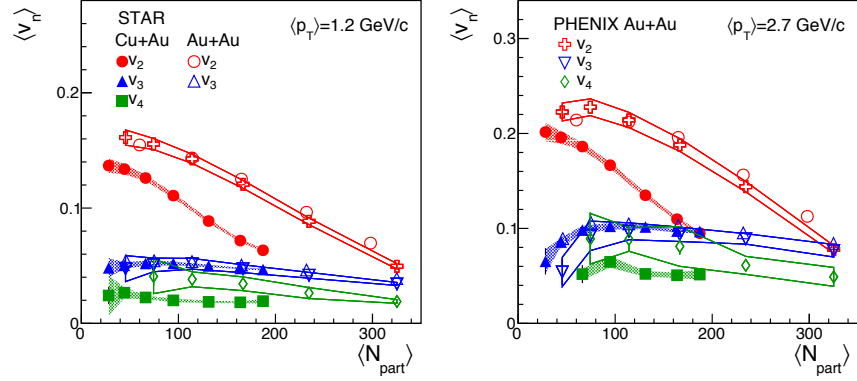
Fig. 31: v_n as a function of the number of participants N_{part} for two selected p_T bins. Results for Au+Au collisions from the STAR and PHENIX are compared.
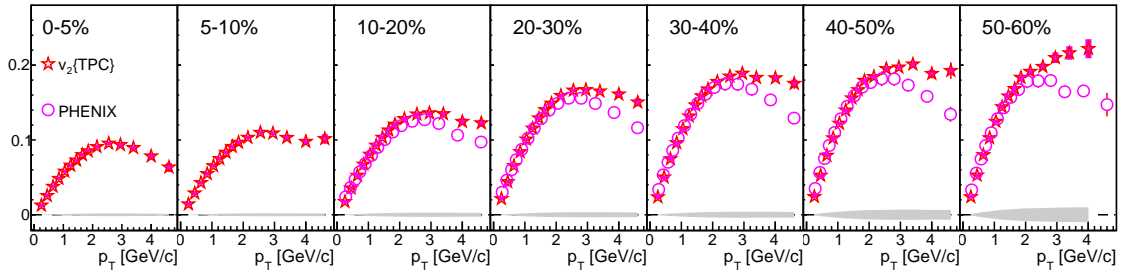
Fig. 32: Comparison of $v_2(p_T)$ with the PHENIX results [11]
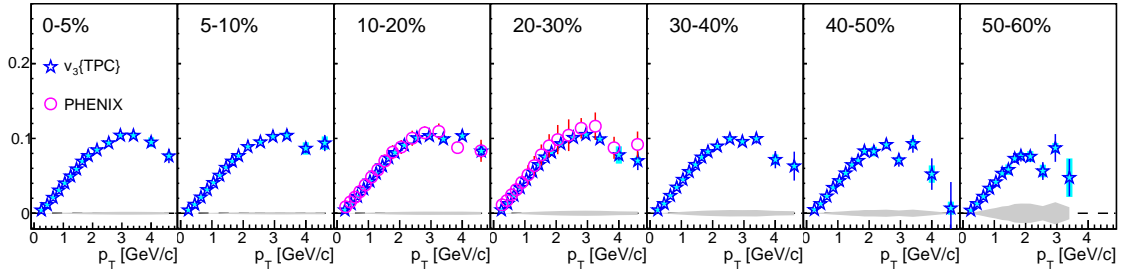
Fig. 33: Comparison of $v_3(p_T)$ with the PHENIX results [11]
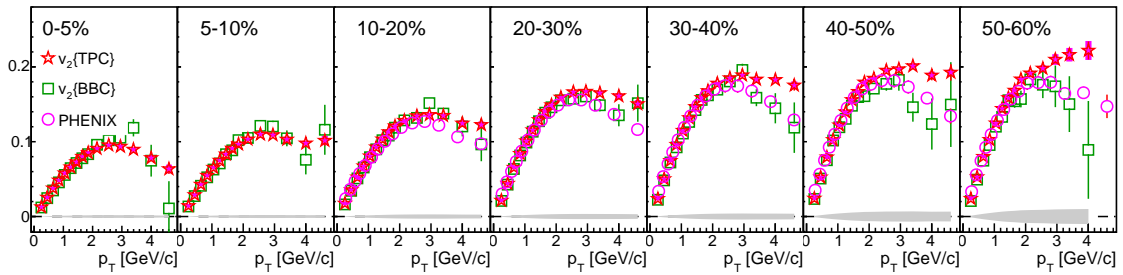
Fig. 34: Comparison of $v_2(p_T)$ with the PHENIX results [11]
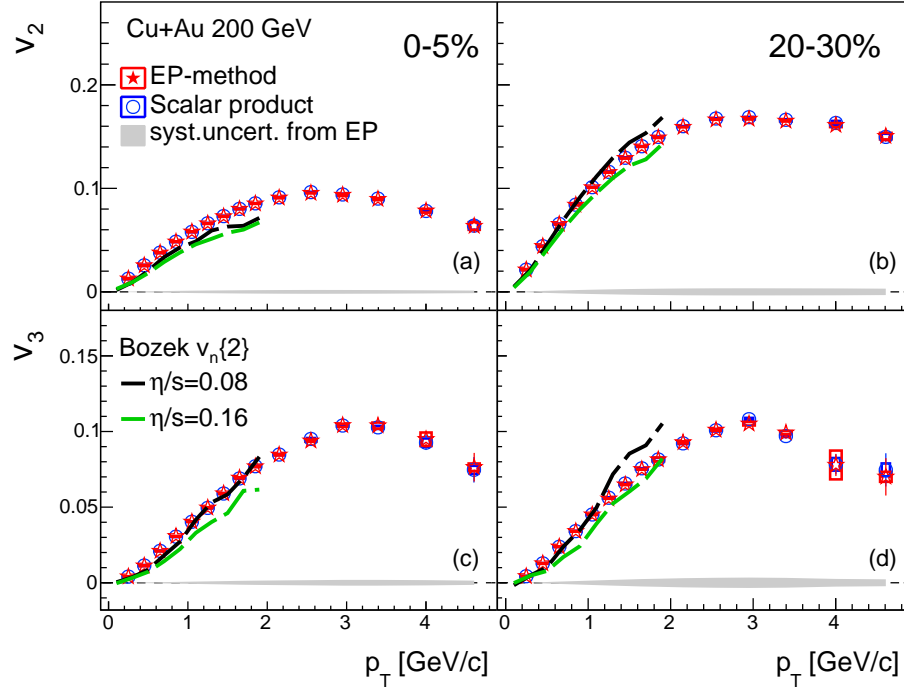
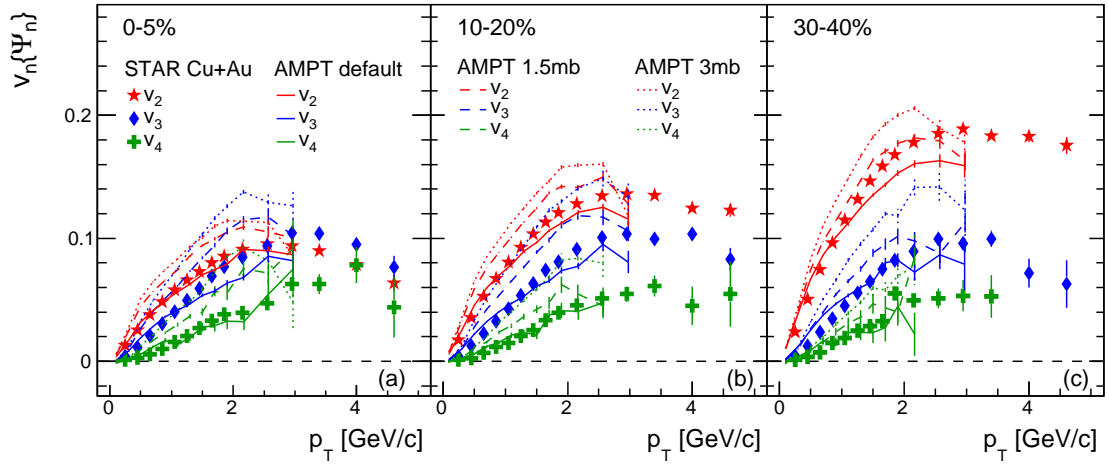Fig. 35: Comparison of $v_2(p_T)$ and $v_3(p_T)$ with the event-by-event viscous hydrodynamic model [12]

Fig. 36: Comparison of $v_2(p_T)$, $v_3(p_T)$ and $v_4(p_T)$ with AMPT models calculated with the default version and string melting version for $\sigma_{pp} = 1.5$ mb and $\sigma_{pp} = 3$ mb.

3.2   Identified charged particles

Figure 37 shows v_1 of $\pi^+ + \pi^-$, $K^+ + K^-$, and $p + \bar{p}$ as a function of p_T in 10-40% centrality bin. Here the v_1 was measured with respect to Au-going spectator plane. Therefore note that the fluctuation component that we defined is included. Particle mass dependence is observed at $p_T < 2$ GeV/c, which has been also observed in the AGS experiment [16] and could be explained by the radial flow.
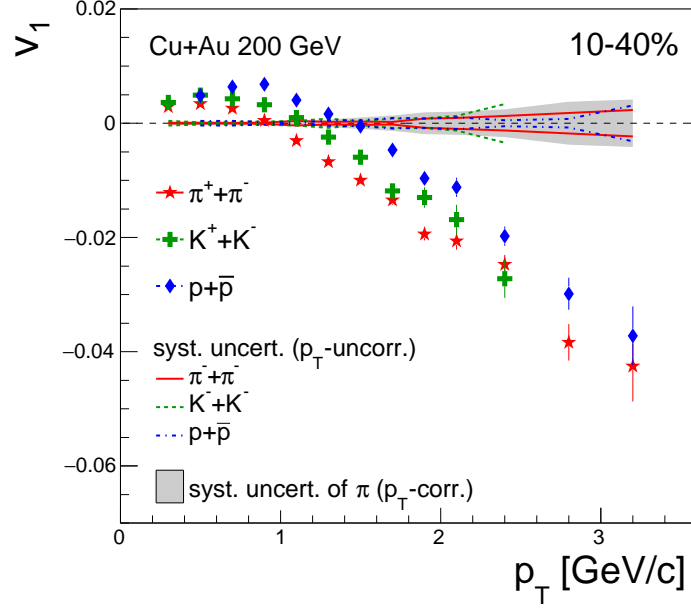

Fig. 37: v_1 of $\pi^+ + \pi^-$, $K^+ + K^-$, and $p + \bar{p}$ as a function of p_T for 10-40% central Cu+Au collisions.

Figure 38 shows p_T dependence of v_2 and v_3 of charged pions, kaons and (anti)protons for different centrality bins. Particles mass dependence at $p_T < 1.6 \sim 2$ (slightly different with centrality) and baryon/meson splitting at intermediate p_T can be seen as observed in Au+Au collisions. The statistics was not enough to perform v_4 measurement with fine centrality bin, but the measurement is still possible for a wide centrality bin as shown in Fig. 39. It seems that the similar trend is also seen in v_4.
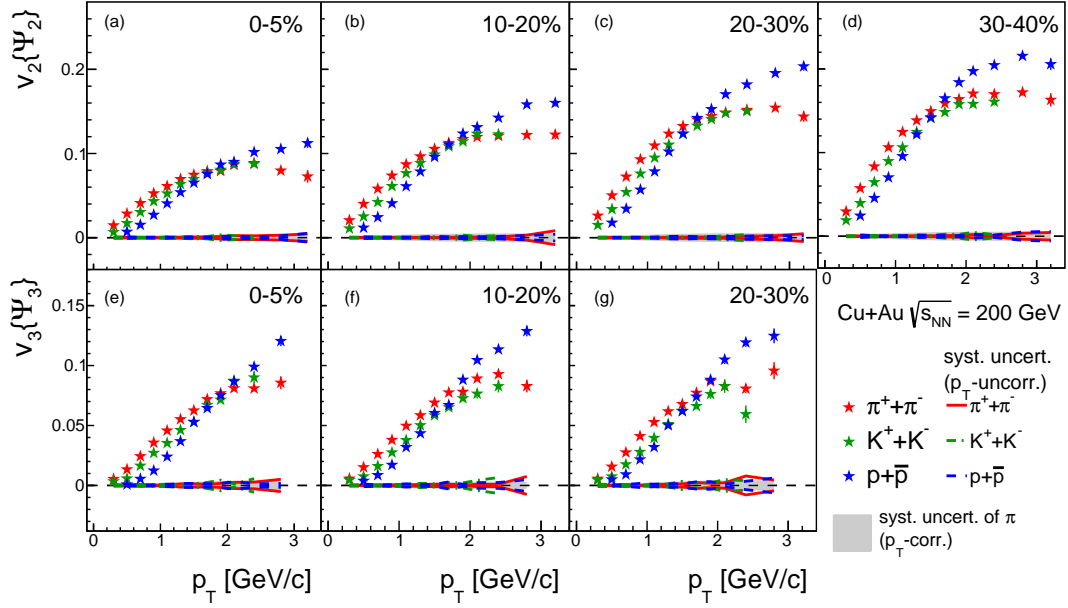
Fig. 38: v_2 and v_3 of $\pi^+ + \pi^-$, $K^+ + K^-$, and $p + \bar{p}$ as a function of p_T for different centrality bins in Cu+Au collisions.
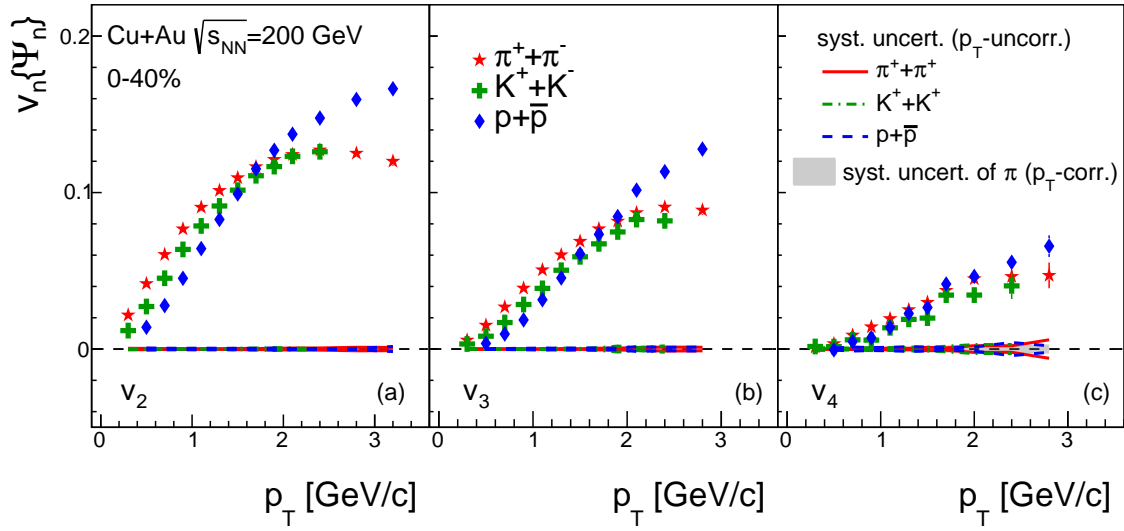
Fig. 39: v_2, v_3, and v_4 of $\pi^+ + \pi^-$, $K^+ + K^-$, and $p + \bar{p}$ as a function of p_T for 0-40% central Cu+Au collisions.

We tested the number of constituent quark (NCQ) scaling for our v_n. Figure 41 (a-c) shows the NCQ scaling for v_n as a function of the kinetic energy defined as $(m_T - m_0)/n_q$. The m_T is defined as $m_T = \sqrt{(p_T^2 + m_0^2)}$, where m_0 denotes a particle mass and n_q denotes the number of constituent quark ($n_q = 2$ for mesons and $n_q = 3$ for baryons). The NCQ scaling works for v_2, but doesn't work well for v_3 and v_4. The modified NCQ scaling for higher-orders has been recently proposed by the PHENIX experiment [17]. In that scaling, $v_n/n_q^{n/2}$ is applied instead of v_n/n_q. Figure 41 (d,e) shows the modified NCQ scaling for v_3 and v_4 (Note that the scaling for v_2 doesn't change). The modified NCQ scaling works better for v_3 and v_4. We also checked the NCQ scaling using p_T instead of using the kinetic energy. The scaling slightly becomes worse but it works to some extent without the "modification" of scaling.
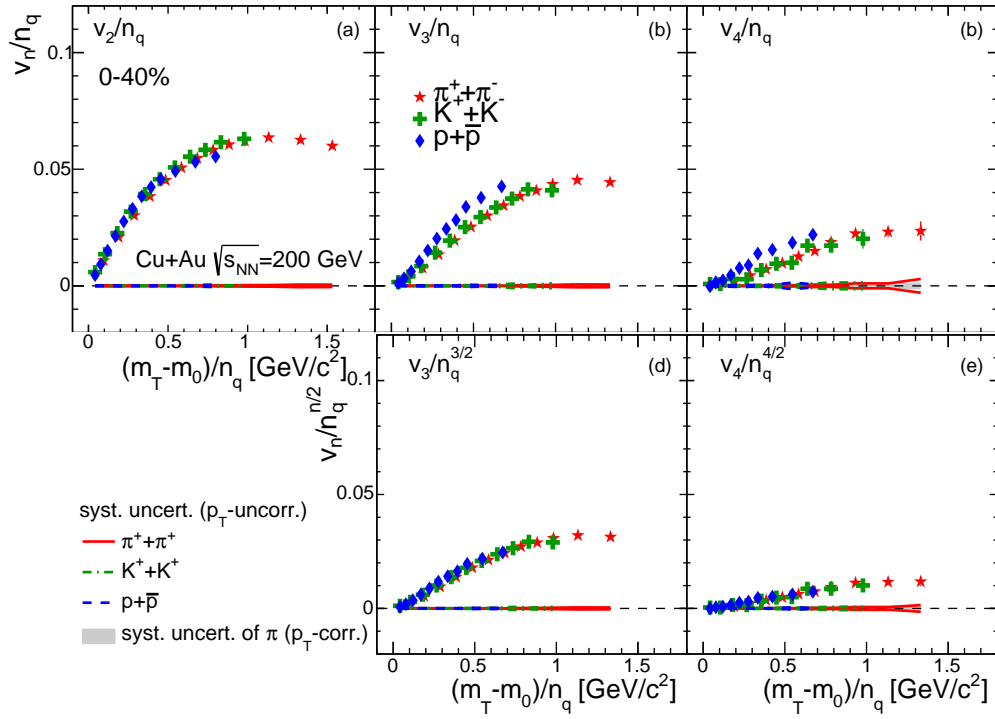
Fig. 40: v_n/n_q and $v_n/n_q^{n/2}$ versus $(m_T - m_0)/n_q$ for $\pi^+ + \pi^-$, $K^+ + K^-$, and $p + \bar{p}$ for 0-40% central Cu+Au collisions.
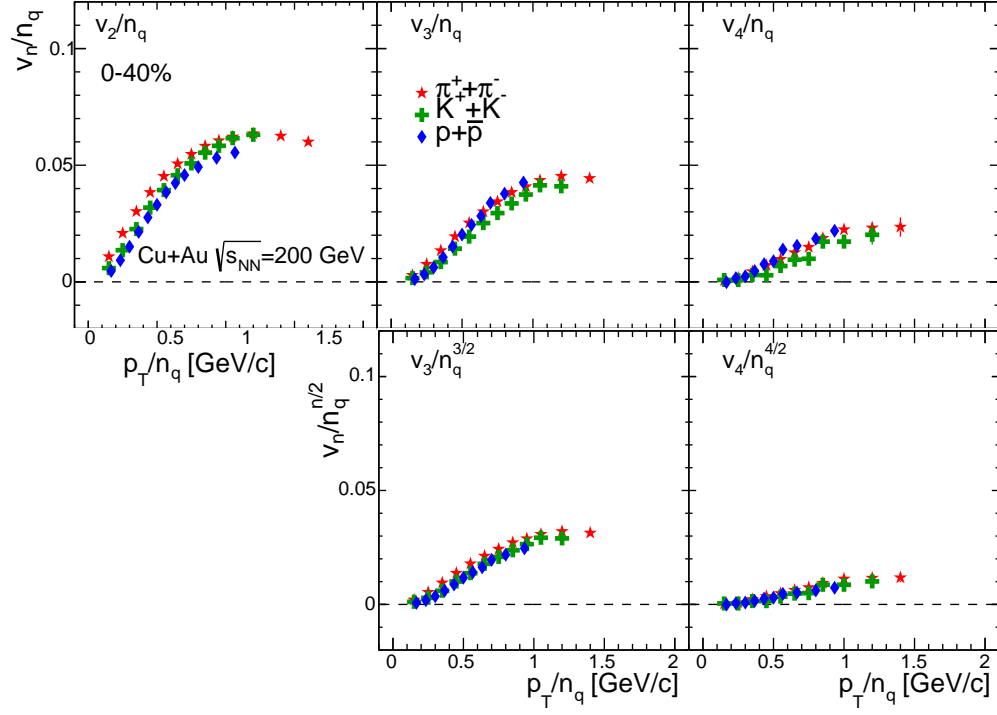
Fig. 41: v_n/n_q and $v_n/n_q^{n/2}$ versus p_T/n_q for $\pi^+ + \pi^-$, $K^+ + K^-$, and $p + \bar{p}$ for 0-40% central Cu+Au collisions.

A   Charge-dependent directed flow for identified particles

Charge-dependent directed flow of charged particles was measured to study the effect of the initial electric field created by charge difference of spectator protons in Cu+Au collisions. Particle dependence of Δv_1 was also studied ($\Delta v_1 = v_1^+ - v_1^-$ where $+(-)$ denotes positively (negatively) charged particles). Figure 42 shows $v_1(p_T)$ and $\Delta v_1(p_T)$ for pions, kaons, and (anti)protons as a function of p_T in 10-40% centrality bin. Pion Δv_1 clearly shows positive value at $p_T < 2$ GeV/c which is similar magnitude and p_T dependence to what has been observed for inclusive charged particles. For kaons and protons, they are consistent with zero or comparable to pion results due to large uncertainties.
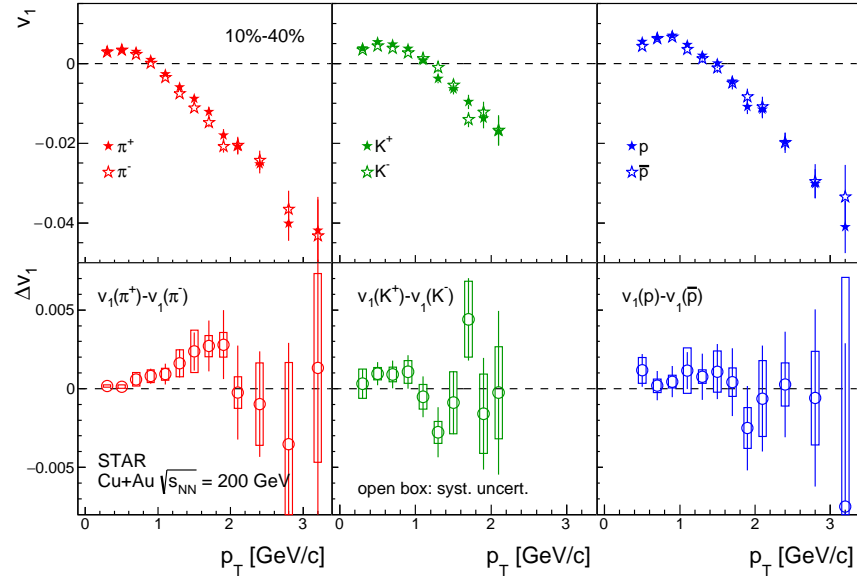

Fig. 42: v_1 and Δv_1 for π, K, and $p(\bar{p})$ as a function of p_T for 10-40% centrality bin in Cu+Au collisions. Only statistical uncertainties are shown for top panels. Open boxes in bottom panes show systematic uncertainties.

The systematic uncertainties for Δv_1 in Fig. 42 were estimated in the same way as in Sec. 2.6. Figure 43 shows Δv_1 for different systematic sources.
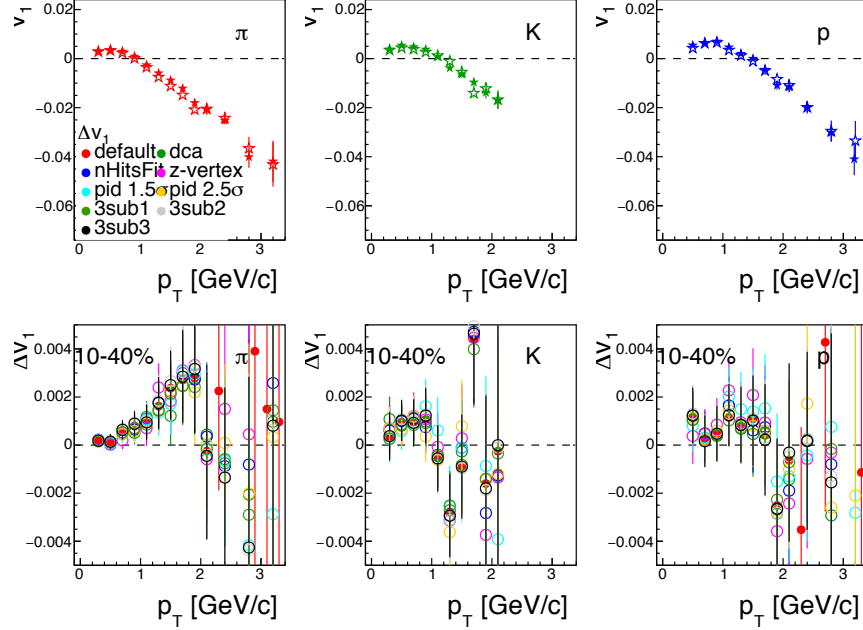
Fig. 43: Systematic study of Δv_1 for π, K, and $p(\bar{p})$ as a function of p_T for 10-40% centrality bin in Cu+Au collisions.

B   Slopes and intercepts of $v_1(\eta)$ and $\langle p_x \rangle / \langle p_T \rangle (\eta)$

Figure 44 and Fig. 45 show v_1 and $\langle p_x \rangle / \langle p_T \rangle$ as a function of η. To extract the slopes and intercepts of them, the data were fitted with a linear function. Just for a cross check, the data measured with respect to ZDCE and ZDCW were also fitted saperately. Since the $\langle p_x \rangle / \langle p_T \rangle$ seems not to follow the linear function over η, we also tested the function of $p_0 + p_1 exp(-p_2 x)$ where p_n are free parameters. The extracted slopes and intercepts are presented as a function of centrality in Fig. 46 and Fig. 47. There was no significant difference between results of two fitting functions. Figure 48 shows the obtained fitting parameter p_2. In 10%-40% centrality bin, the p_2 shows non-zero values.

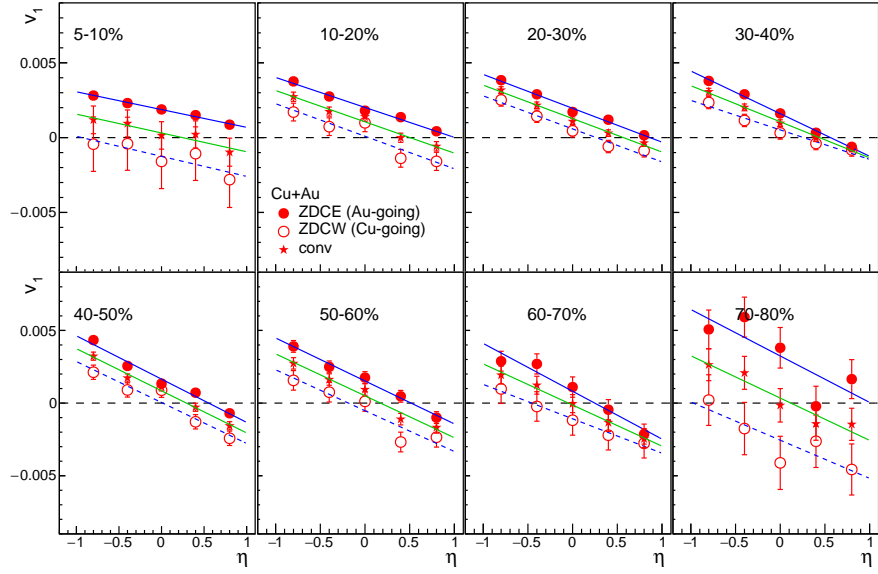The corresponding plots for Au+Au collisions are shown in Fig. 49–52.

Fig. 44: v_1 as a function of η in different centrality bins in Cu+Au collisions.
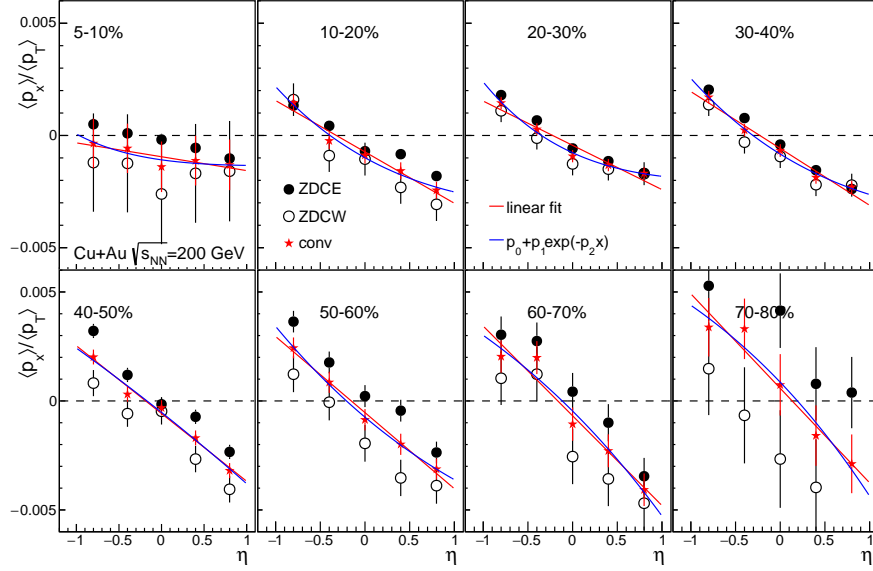
Fig. 45: $\langle p_x \rangle / \langle p_T \rangle$ as a function of η in different centrality bins in Cu+Au collisions.
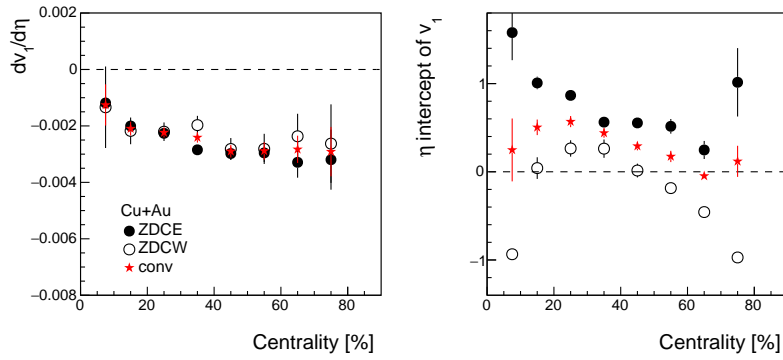

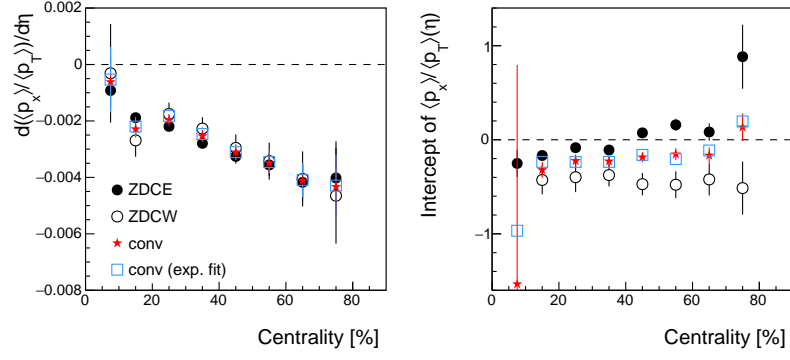Fig. 46: Slopes and inctercepts of v_1 as a function of centrality in Cu+Au collisions.

Fig. 47: Slopes and intcercepts of $\langle p_x \rangle / \langle p_T \rangle$ as a function of centrality in Cu+Au collisions.
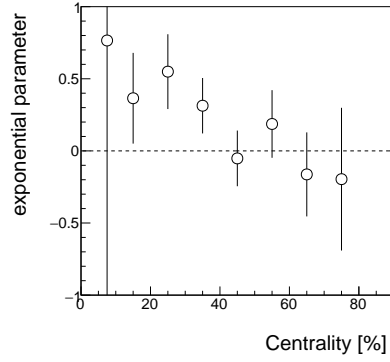

Fig. 48: Exponential parameter in the fit to $\langle p_x \rangle(\eta)/\langle p_T \rangle$ as a function of centrality in Cu+Au collisions.
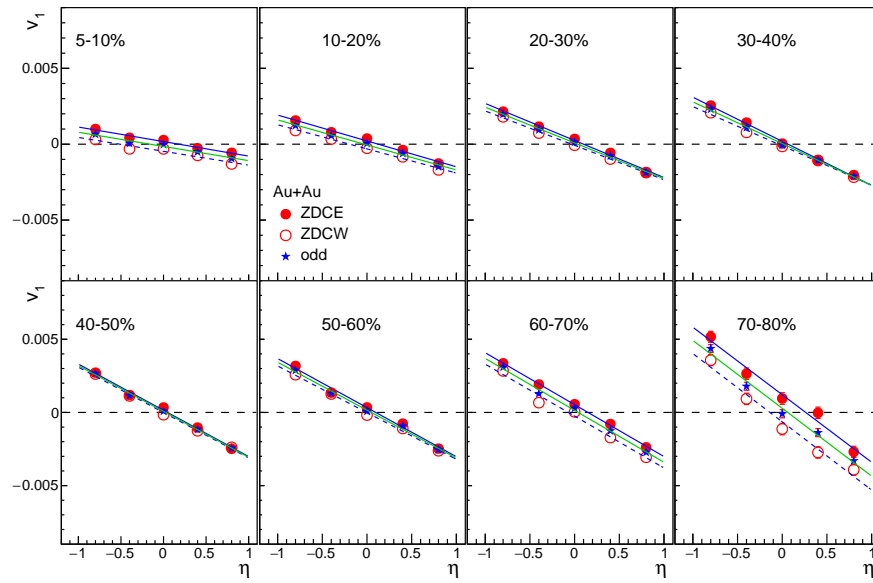
Fig. 49: v_1 as a function of η in different centrality bins in Au+Au collisions.
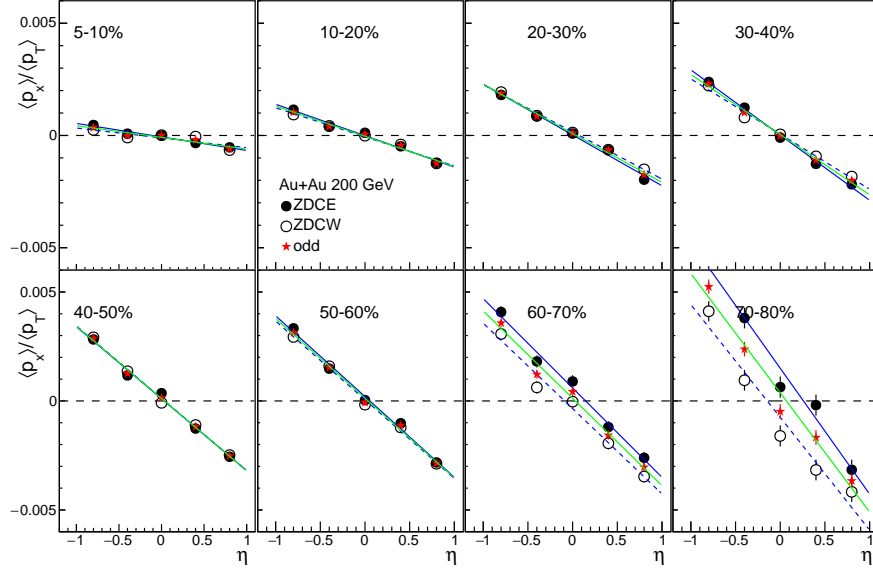
Fig. 50: $\langle p_x \rangle / \langle p_T \rangle$ as a function of η in different centrality bins in Au+Au collisions.
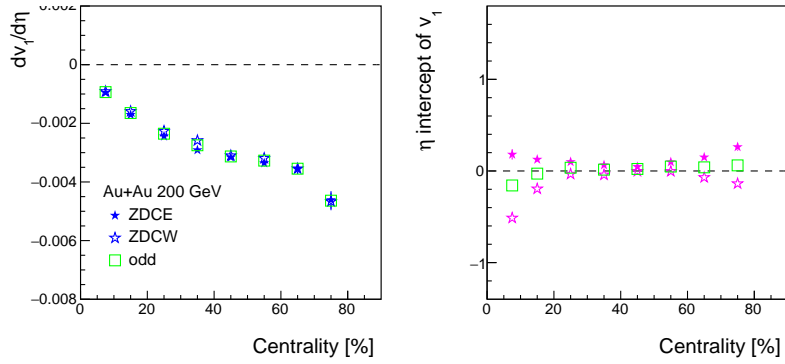

Fig. 51: Slopes and inctercepts of v_1 as a function of centrality in Au+Au collisions.
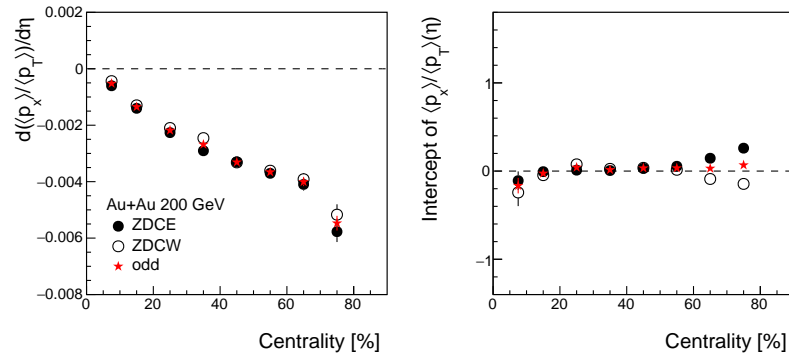
Fig. 52: Slopes and inctercepts of $\langle p_x \rangle / \langle p_T \rangle$ as a function of centrality in Au+Au collisions.

C Particle Identification with TOF

As mentined in the analysis part of this note, the purity was estimated assuming that the signal distributions follow Gaussian functions. Figure 53 shows the mass square distributions after applying $n\sigma_K^{TPC}$ for differetn p_T bins, as an example to estimate the purity of kaon samples. Each π, K, and p peaks were fitted with tripple Gaussian function. In this case, the estimated purity of our kaon samples is about 97%. At higher
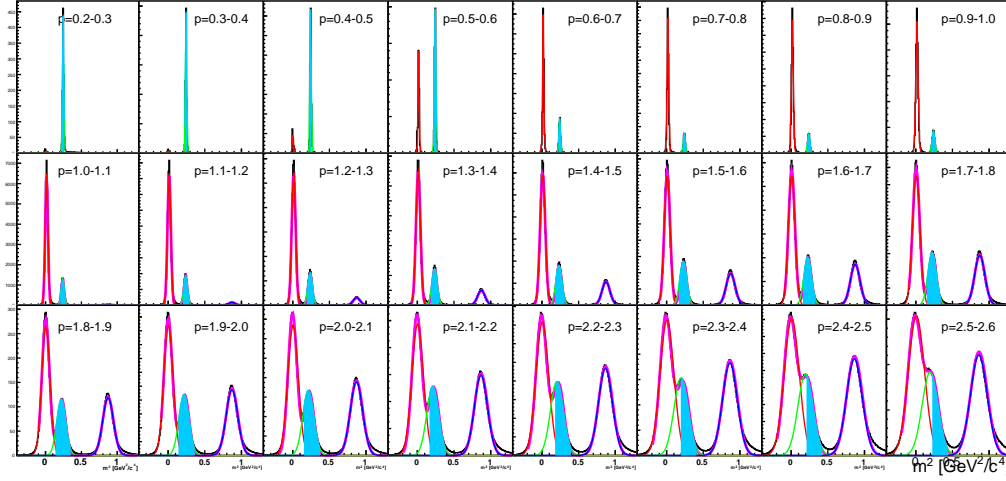

Fig. 53: m^2 distributions after requiring $n\sigma_K^{TPC} < 3$ for different p_T bins with Gaussian fits.

p_T, non-Gaussian tail can be seen for each particles. It might be due to the background caused by mis-reconstructed tracks and/or the Gaussian assumption used here may not be perfect. Note that we could use other function for the fit such as a student t-distribution just for better describing the data, but it is also one of assumptions and does not mean it leads to more acurate estimate of the purity. We also tried to use another fit function including the background distiburion. Figure 54 shows the same data as Fig. 53 but performed the fit with four Gaussian function where fourth Gaussian corresponds to the background. As shownd in Fig. 54, the non-Gaussian tail at higher p_T was described better than Fig. 53. This would be close to the worst case of purity estimate because we assume that all the non-Gaussian part comes from the background. In this case, the estimated purity goes down to ∼90% which is the lowest limit of acceptable purity.

Also, note that variation of PID cuts is taken into account in the systematic uncertainties as shown in Fig. 18 and Fig. 20. Any systematic difference was not seen at higher p_T by the variation.
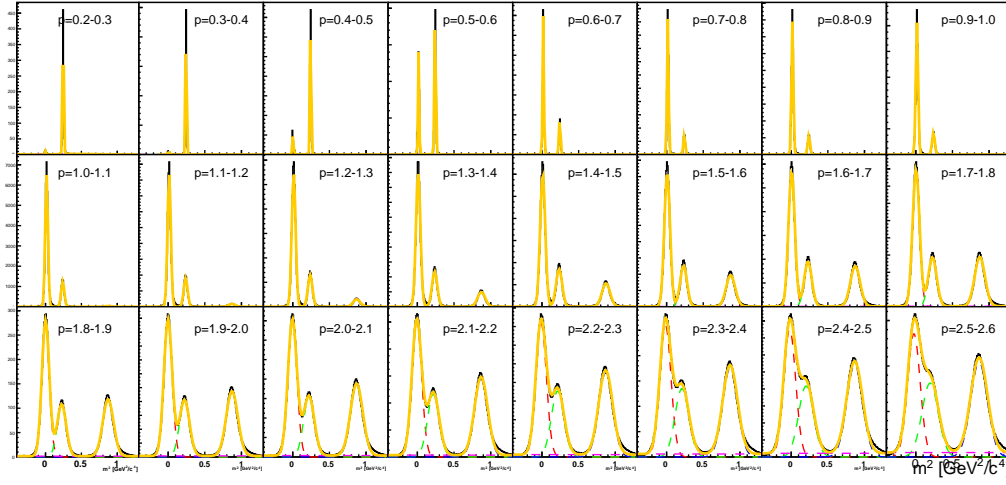
Fig. 54: m^2 distributions after requiring $n\sigma_K^{TPC} < 3$ for different p_T bins with Gaussian fits including the background function.

References

[1] T. Niida and S. Voloshin, STAR Analysis Note PSN0652, Charge-dependent directed flow in Cu+Au collisions at $\sqrt{s_{NN}}$=200 GeV

[2] L. Adamczyk *et al.* (STAR Collaboration), Phys. Rev. Lett. **118**, 012301 (2017)

[3] B. Abelev *et al.* (ALICE Collaboration), Phys. Rev. Lett. **111**, 232302 (2013)

[4] L. Adamczyk *et al.* (STAR Collaboration), "Phys. Rev. Lett. **112**, 162301 (2014)

[5] Y. Hirono, M. Hongo, and T. Hirano, Phys. Rev. C **90**, 021903 (2014)

[6] V. Voronyuk, V. D. Toneev, S. A. Voloshin, and W. Cassing, Phys. Rev. C **90**, 064903 (2014)

[7] J. Barrette *et al.* (E877 Collaboration), Phys. Rev. C **56**, 3254 (1997)

[8] J. Barrette *et al.* (E877 Collaboration), Phys. Rev. C **55**, 1420 (1997)

[9] A. M. Poskanzer and S. A. Voloshin, Phys. Rev. C **58**, 1671 (1998)

[10] J. Adams *et al.* (STAR Collaboration), Phys. Rev. C **73**, 034903 (2006)

[11] A. Adare *et al.* (PHENIX Collaboration), arXiv:1509.07784 (2015)

[12] P. Bożek, Phys. Lett. B **717**, 287 (2012)

[13] J. Adams *et al.* (STAR Collaboration), Phys. Rev. C **72**, 465 014904 (2005).

[14] J. Adams *et al.* (STAR Collaboration), Phys. Rev. C **88**, 473 014904 (2013)

[15] A. Adare *et al.* (PHENIX Collaboration), Phys. Rev. Lett. **107**, 252301 (2011)

[16] S. A. Voloshin (E877 Collaboration), Nucl. Phys. A **638**, 455c (1998)

[17] A. Adare et al. (PHENIX Collaboration), Phys. Rev. C 93, 051902(R) (2016)